Monthly Notices
of the
ROYAL ASTRONOMICAL SOCIETY

MNRAS **440,** 405–426 (2014)
Advance Access publication 2014 March 11

doi:10.1093/mnras/stu199

A Council of Giants

Marshall L. McCall★

Department of Physics and Astronomy, York University, Toronto, Ontario L3T 3R1, Canada

Accepted 2014 January 28. Received 2013 December 31; in original form 2013 April 29

ABSTRACT

Distances and near-infrared luminosities of the brightest galaxies in the Local Volume have been re-evaluated in order to gain a fully homogeneous collection of data for elucidating the framework of the Local Sheet and its relevance to Local Group evolution. It is demonstrated that the Local Sheet is both geometrically and dynamically distinct from the Local Supercluster and that the evolution of the Sheet and Local Group were probably interconnected. The Sheet is inclined by 8° with respect to the Local Supercluster, and the dispersion of giant members about the mid-plane is only 230 kpc. A 'Council of Giants' with a radius of 3.75 Mpc encompasses the Local Group, demarcating a clear upper limit to the realm of influence of the Local Group. The only two giant elliptical galaxies in the Sheet sit on opposite sides of the Council, raising the possibility that they have somehow shepherded the evolution of the Local Group. The position vector of the Andromeda galaxy with respect to the Milky Way deviates only 11° from the Sheet plane and only 11° from the projected axis of the ellipticals. The Local Group appears to be moving away from a ridge in the potential surface of the Council on a path parallel to the elliptical axis. Spin directions of the giants in the Council are distributed over the sky in a pattern which is very different from that of giants beyond, possibly in reaction to the central mass asymmetry that developed into the Local Group. By matching matter densities of Group and Council giants, the edge of the volume of space most likely to have contributed to the development of the Local Group is shown to be very close to where gravitational forces from the Local Group and the Council balance. The boundary specification reveals that the Local Sheet formed out of a density perturbation of very low amplitude (∼10 per cent), but that normal matter was incorporated into galaxies with relatively high efficiency (∼40 per cent). It appears that the development of the giants of the Local Sheet was guided by a pre-existing flattened framework of matter.

Key words: galaxies: distances and redshifts – galaxies: evolution – galaxies: formation – galaxies: kinematics and dynamics – Local Group – large-scale structure of Universe.

1 INTRODUCTION

Galaxies are organized into an expanding cosmic web of filamentary and sheet-like structures bounding volumes which are largely devoid of matter. However, very little is known observationally about the structure of structures and its linkages to galaxy evolution because it is difficult to constrain accurate relative positions of constituents from a distant vantage point. The Local Sheet, a structure of which we are a part, offers an opportunity for advancement owing to our perspective from within and the proximity to measure reliable distances to members directly.

Any study of local structure must start with a volume-limited sample of galaxies. Efforts to construct such a sample began with the definition of the Local Volume (Kraan-Korteweg & Tammann 1979; Huchtmeier & Richter 1986; Schmidt & Boller 1992a), which in the rendition initiating this work (the Local Volume Catalog, or LVC – Karachentsev et al. 2004) contains all known galaxies either with distances less than 10 Mpc or with radial velocities less than 550 km s^{-1} with respect to the Local Group (a Hubble flow distance of 7.7 Mpc). Within the Local Volume, the Milky Way, Andromeda, and the smaller companions which comprise the Local Group reside in a layer of galaxies, mostly dwarfs, which has an apparent thickness of about 1.5 Mpc (Schmidt & Boller 1992b; Peebles 1993; Peebles et al. 2001; Karachentsev et al. 2004; Karachentsev 2005; Tully et al. 2008; Fingerhut 2012). At various times, the layer has been referred to as the 'Local Cloud' (de Vaucouleurs 1975), the 'Coma-Sculptor Cloud' (Tully & Fisher 1987), the 'local plane' (Peebles 1993), the 'local filament' (Klypin et al. 2003), the 'Local pancake' (Karachentsev et al. 2004), and the 'Local Sheet' (Peebles et al. 2001; Tully et al. 2008; Peebles & Nusser 2010). At a certain level, it is the proximate manifestation of the Local Supercluster, whose existence was in fact established in part using

★ E-mail: mccall@yorku.ca

the most luminous members of the layer (de Vaucouleurs 1953). However, models of the local velocity field seem to require that the Local Group be housed in a flattened body of galaxies distinct from the Local Supercluster (Klypin et al. 2003). Indeed, it has been argued that the supergalactic arrangement of nearby groups in the plane of the sky is evidence for such a body (de Vaucouleurs 1975). Also, peculiar velocities of galaxies show a sharp discontinuity at a distance of about 7 Mpc (Tully et al. 2008). Studies of local structure are traditionally anchored to the supergalactic coordinate system, but whether or not this is the appropriate framework to adopt has not been examined thoroughly.

Any local flattened structure distinct from the Local Supercluster ought to be traced most reliably by its most luminous members, because they pinpoint the location of the largest concentrations of dark matter. Consequently, to isolate such a structure and elucidate its character, this paper focuses on carefully mapping the distribution and properties of luminous spiral and elliptical galaxies in the Local Volume. The framework is vital for guiding studies of the dwarf population locally (Fingerhut 2012), results from which will be presented separately.

2 SAMPLE

A sample of luminous galaxies in the Local Volume was constructed primarily from the LVC. For a galaxy to be included in the sample, it was required that the tabulated absolute magnitude in B be equal to or brighter than -18.0. The adopted luminosity cut-off is fully 3 mag brighter than the median absolute magnitude of galaxies near the edge of the LVC (8 to 10 Mpc). This means that LVC selection criteria, not survey detection thresholds, determine the representation of galaxies. Furthermore, the cut-off is comparable to the brightness of the largest dwarfs (e.g. the Large Magellanic Cloud). Thus, it is faint enough to ensure that true giants, as defined by stellar mass, are completely sampled, even accounting for possible errors in LVC distances or biasing of blue luminosities by star formation.

A total of 56 galaxies in the LVC satisfied the brightness criterion. Added to the sample were the M33-like spiral NGC 300, which was listed in the LVC as being slightly fainter than the absolute magnitude cut-off, and NGC 1023, NGC 4631, and NGC 5023, which modern distance determinations seemed to place within 10 Mpc. Thus, the final sample comprised 60 galaxies. After re-evaluating all distances and brightnesses, seven galaxies proved to be fainter than the absolute magnitude cut-off, and six lay beyond the nominal distance limit.

Sample galaxies are listed with their properties in Table 1, and the sources of the observations underlying the tabulated parameters are identified in Table 2. All distance-dependent quantities are anchored to the nuclear maser distance for M106 (Humphreys et al. 2013). Details about the origins and usage of tabulations are given in the sections to follow. Listed uncertainties, which are standard deviations, account for all random sources of error, but they exclude the error in the distance zero-point (where relevant) because it is systematic. Thus, the errors reflect how uncertain a property of one galaxy is with respect to that of any other.

3 METHOD

3.1 Motions

To study the kinematics of the Local Group with respect to neighbouring galaxies, the heliocentric line-of-sight velocity of each galaxy was adopted, whenever possible, to be a published measurement of the systemic velocity derived by fitting a map of the internal velocity field. Measurements made this way were preferred to those from integrated spectral line profiles because they are less susceptible to perturbation by asymmetries in the spatial distribution of matter, particularly in the case of neutral hydrogen.

For galaxies beyond the Local Group, the heliocentric velocity was corrected for local expansion using a value for the Hubble constant founded upon infrared observations of Cepheids and a period–luminosity relation anchored to the distance of M106 (Riess et al. 2011, 2012). After accounting for the recent revision to the maser distance to M106 (Humphreys et al. 2013), the following value for the Hubble constant was adopted: $H_0 = 71.6 \pm 2.9\,\mathrm{km\,s^{-1}\,Mpc^{-1}}$. To place a velocity in the frame of reference of the Local Group, the reflex motion of the Sun with respect to the luminosity-weighted centroid (in K_s) of the Local Group was removed using modern determinations of the motion of the Sun with respect to the Local Standard of Rest (Schönrich, Binney & Dehnen 2010), the orbital velocity of the Local Standard of Rest about the Milky Way (McMillan 2011; van der Marel et al. 2012), and the orbital motion of Andromeda with respect to the Sun (van der Marel et al. 2012) after appropriately correcting the tangential component for the revision to the distance to Andromeda presented in Table 1. For kinematic studies of galaxies beyond the Local Group, each interacting pair (Maffei 1 and 2; M81 and M82) was regarded as a single unit moving at the luminosity-weighted mean velocity of its constituents.

Internal ordered motions were characterized by the rotational velocity in the plateau of the rotation curve. When possible, this was judged from a published fit to the internal velocity field. However, for NGC 5068 and E274-G001, the rotational velocity had to be gauged from the H I line width at 20 per cent of the peak flux, and for M74 (NGC 628), which is almost face-on, the rotational velocity was estimated from the absolute magnitude in K_s using the Tully–Fisher relation.

3.2 Orientations

The orientation of each sample galaxy, i.e. the tilt of the spin axis relative to the line of sight and the position angle of the line of nodes, had to be constrained to correct magnitudes for internal extinction (in the case of a disc galaxy), to correct the apparent rotational velocity for projection, and to evaluate the direction of the angular momentum vector of the optical disc. In this paper, the position angle is measured east from north to the nearest limb, and thereby takes on values between 0° and 180°.

For a disc galaxy, one gauge of tilt is the ratio of the semi-minor to the semi-major axis of the disc, better known as the axis ratio. It was established where possible from the outermost isophotes of the deepest optical maps of surface brightness in the reddest possible passbands, and otherwise from the compilation of HyperLeda (Paturel et al. 2003). The corresponding tilt was derived assuming that discs are oblate spheroids with an edge-on axis ratio q_0 dependent on the Revised Hubble Type T as follows:

$$\begin{aligned} q_0 &= 0.20 \quad -3.5 < T < 3.5 \\ &= 0.13 \quad 3.5 \leq T < 9.5 \\ &= 0.57 \quad 9.5 \leq T \end{aligned} \tag{1}$$

(Sakai et al. 2000; Staveley-Smith, Davies & Kinman 1992; see also Verheijen 1997). Also, where possible, independent estimates of tilt were acquired from extant fits to maps of velocity fields.

Table 1. Galaxies in the sample.

Galaxy $L_{\rm sheet}$ $B_{\rm sheet}$ (1)	T $V_\odot$ $V_{\rm LG}$ (2)	τ_1 DM Method (3)	$X_{\rm sheet}$ $Y_{\rm sheet}$ $Z_{\rm sheet}$ (4)	M_{Ks} M_V $B-V$ (5)	$\log \mathcal{M}_{\rm stars}$ i PA (6)	$V_{\rm flat}$ $L_{\rm sheet}(AM)$ $B_{\rm sheet}(AM)$ (7)
NGC 55	8.7	0.015 ± 0.002	−1.756 ± 0.040	−21.36 ± 0.23	9.445 ± 0.092	84 ± 2
211.30	120.5 ± 3.0	26.573 ± 0.050	−1.067 ± 0.025	−18.96 ± 0.07	81.2 ± 1.6 (−)	112.7 ± 1.6
8.87	−51.6 ± 6.3	C,T	0.321 ± 0.004	0.425 ± 0.050	105.0 ± 4.0 (+)	−2.2 ± 4.0
Andromeda	3.0	0.070 ± 0.011	0.296 ± 0.013	−24.94 ± 0.25	11.042 ± 0.101	226 ± 5
292.90	−301.0 ± 1.0	24.453 ± 0.093	−0.701 ± 0.030	−22.17 ± 0.13	78.0 ± 0.5 (−)	198.8 ± 0.9
20.72	−62.5 ± 9.8	C,P,S,T	0.288 ± 0.007	0.652 ± 0.041	37.9 ± 0.5 (+)	−54.8 ± 0.5
NGC 247	6.9	0.020 ± 0.003	−2.420 ± 0.087	−21.84 ± 0.26	9.648 ± 0.103	105 ± 7
230.89	161.0 ± 7.0	27.922 ± 0.078	−2.976 ± 0.107	−19.41 ± 0.14	74.8 ± 0.8 (+)	173.9 ± 1.8
4.76	−72.5 ± 12.7	T	0.320 ± 0.007	0.440 ± 0.050	170.6 ± 0.5 (+)	66.5 ± 0.6
NGC 253	5.1	0.022 ± 0.003	−2.382 ± 0.049	−24.37 ± 0.05	10.805 ± 0.019	217 ± 4
226.46	236.0 ± 1.0	27.695 ± 0.045	−2.506 ± 0.052	−21.40 ± 0.07	75.9 ± 0.9 (+)	297.2 ± 1.4
4.02	10.0 ± 6.6	P,T	0.243 ± 0.002	0.638 ± 0.050	51.1 ± 0.5 (−)	48.6 ± 0.5
NGC 300	6.9	0.015 ± 0.002	−1.687 ± 0.062	−21.19 ± 0.26	9.468 ± 0.103	94 ± 8
214.56	144.5 ± 3.0	26.558 ± 0.080	−1.162 ± 0.043	−18.59 ± 0.14	46.4 ± 3.6 (−)	348.5 ± 3.6
1.66	−37.8 ± 7.3	C,P,T	0.059 ± 0.003	0.550 ± 0.050	106.8 ± 1.2 (−)	−3.6 ± 0.9
M33	6.0	0.048 ± 0.008	0.207 ± 0.007	−21.77 ± 0.24	9.636 ± 0.096	106 ± 4
283.49	−180.0 ± 1.0	24.741 ± 0.078	−0.863 ± 0.031	−19.30 ± 0.10	54.0 ± 0.5 (+)	299.8 ± 0.7
8.60	11.8 ± 8.9	C,P,T	0.134 ± 0.000	0.462 ± 0.021	22.5 ± 0.5 (−)	52.6 ± 0.5
M74	5.2	0.080 ± 0.013	−0.160 ± 0.005	−23.14 ± 0.09	10.196 ± 0.034	147 ± 16
268.97	655.5 ± 1.5	29.759 ± 0.067	−8.936 ± 0.276	−20.85 ± 0.27	9.3 ± 0.9 (+)	266.6 ± 0.8
−2.17	162.8 ± 15.8	P	−0.339 ± 0.014	0.482 ± 0.015	25.0 ± 5.0 (+)	−11.9 ± 0.8
NGC 672	6.0	0.089 ± 0.014	1.094 ± 0.175	−20.54 ± 0.35	9.140 ± 0.141	78 ± 5
280.92	422.0 ± 2.0	28.810 ± 0.348	−5.666 ± 0.909	−18.12 ± 0.37	64.3 ± 0.7 (+)	219.5 ± 1.2
−2.01	182.8 ± 50.9	TF in I	−0.202 ± 0.053	0.457 ± 0.052	67.5 ± 3.5 (+)	−32.3 ± 3.1
NGC 891	3.0	0.074 ± 0.012	4.592 ± 0.207	−24.66 ± 0.10	10.856 ± 0.040	227 ± 5
297.21	528.0 ± 2.0	30.022 ± 0.098	−8.931 ± 0.403	−21.54 ± 0.21	88.3 ± 1.5 (−)	340.3 ± 10.2
−5.52	−6.8 ± 31.4	P,T	−0.971 ± 0.050	0.551 ± 0.051	22.5 ± 0.5 (−)	83.8 ± 1.1
NGC 925	6.9	0.086 ± 0.014	3.081 ± 0.068	−22.30 ± 0.07	9.819 ± 0.029	112 ± 6
289.10	546.3 ± 3.9	29.902 ± 0.048	−8.899 ± 0.197	−20.30 ± 0.14	61.0 ± 5.0 (+)	350.6 ± 5.0
−9.13	27.0 ± 15.8	C	−1.513 ± 0.036	0.424 ± 0.052	109.3 ± 2.7 (−)	−6.0 ± 2.4
NGC 1023	−2.7	0.069 ± 0.011	4.558 ± 0.357	−24.16 ± 0.17	10.935 ± 0.069	237 ± 30
295.25	617.0 ± 1.0	30.181 ± 0.170	−9.665 ± 0.757	−20.98 ± 0.21	72.2 ± 1.3 (0)	–
−9.87	9.2 ± 54.7	P,S	−1.860 ± 0.156	0.933 ± 0.051	85.0 ± 1.0 (+)	–
Maffei 1	−5.0	1.691 ± 0.066	2.290 ± 0.284	−24.24 ± 0.40	10.928 ± 0.159	–
314.24	66.4 ± 5.0	27.583 ± 0.269	−2.352 ± 0.291	−21.12 ± 0.33	– (0)	–
0.01	41.1 ± 31.2	FP in I	0.000 ± 0.016	0.879 ± 0.133	83.9 ± 0.7 (0)	–
Maffei 2	4.0	2.017 ± 0.211	2.406 ± 0.395	−23.90 ± 0.73	10.493 ± 0.290	170 ± 4
314.45	−23.0 ± 1.0	27.683 ± 0.356	−2.452 ± 0.402	−21.42 ± 0.69	67.0 ± 1.0 (+)	317.0 ± 3.2
−0.74	−61.5 ± 41.7	TF in I	−0.044 ± 0.028	0.470 ± 0.371	24.5 ± 1.5 (−)	64.1 ± 1.0
Dwingeloo 1	6.0	1.710 ± 0.104	2.572 ± 0.294	−22.15 ± 0.46	9.773 ± 0.184	113 ± 4
314.64	107.9 ± 0.4	27.825 ± 0.248	−2.604 ± 0.298	−19.71 ± 0.40	51.0 ± 2.0 (−)	185.4 ± 2.0
−2.90	45.7 ± 31.7	TF in I	−0.185 ± 0.036	0.443 ± 0.096	111.4 ± 0.6 (+)	−0.9 ± 0.6
NGC 1313	7.0	0.124 ± 0.020	−4.019 ± 0.037	−21.67 ± 0.24	9.511 ± 0.096	104 ± 6
183.81	480.0 ± 2.0	28.167 ± 0.020	−0.268 ± 0.002	−19.39 ± 0.10	45.4 ± 2.6 (+)	146.0 ± 4.0
−18.87	−19.2 ± 7.1	T	−1.376 ± 0.014	0.344 ± 0.053	2.5 ± 1.5 (+)	−56.2 ± 1.8
IC 342	5.9	0.677 ± 0.056	2.758 ± 0.117	−23.51 ± 0.10	10.302 ± 0.041	192 ± 22
325.37	25.0 ± 3.0	27.633 ± 0.092	−1.904 ± 0.081	−21.30 ± 0.19	25.0 ± 3.0 (−)	145.7 ± 1.4
−2.41	−19.4 ± 14.3	C,P	−0.141 ± 0.011	0.425 ± 0.065	39.0 ± 3.0 (+)	−20.4 ± 3.0
NGC 1569	9.6	0.804 ± 0.129	2.264 ± 0.033	−19.03 ± 0.11	8.246 ± 0.045	35 ± 4
326.11	−81.6 ± 4.4	27.212 ± 0.032	−1.521 ± 0.022	−18.43 ± 0.37	90.0 ± 1.0 (−)	232.6 ± 0.6
−7.37	−103.9 ± 11.0	T	−0.353 ± 0.007	0.062 ± 0.126	119.3 ± 1.1 (+)	−19.0 ± 1.1
NGC 2403	6.0	0.045 ± 0.007	3.116 ± 0.072	−22.26 ± 0.24	9.791 ± 0.094	134 ± 2
344.94	133.2 ± 2.2	27.620 ± 0.050	−0.838 ± 0.019	−19.87 ± 0.09	60.5 ± 2.5 (+)	287.8 ± 4.4
−12.94	22.8 ± 9.9	C,P	−0.742 ± 0.020	0.409 ± 0.050	125.3 ± 0.8 (+)	−58.9 ± 1.1

Table 1 – *continued*

Galaxy $L_{\rm sheet}$ $B_{\rm sheet}$ (1)	T $V_\odot$ $V_{\rm LG}$ (2)	τ_1 DM Method (3)	$X_{\rm sheet}$ $Y_{\rm sheet}$ $Z_{\rm sheet}$ (4)	M_{Ks} M_V $B-V$ (5)	$\log \mathcal{M}_{\rm stars}$ i PA (6)	$V_{\rm flat}$ $L_{\rm sheet}(AM)$ $B_{\rm sheet}(AM)$ (7)
NGC 2683	3.1	0.037 ± 0.006	5.672 ± 0.933	−23.49 ± 0.36	10.521 ± 0.143	156 ± 8
10.21	415.0 ± 1.0	29.425 ± 0.357	1.022 ± 0.168	−20.62 ± 0.36	79.3 ± 2.1 (+)	294.5 ± 1.8
−40.59	−169.3 ± 55.1	S	−4.938 ± 0.833	0.732 ± 0.050	42.8 ± 1.3 (−)	0.0 ± 1.7
NGC 2784	−2.1	0.244 ± 0.039	−1.339 ± 0.160	−24.04 ± 0.26	10.877 ± 0.104	203 ± 10
104.04	708.0 ± 10.0	30.087 ± 0.259	5.356 ± 0.639	−20.67 ± 0.30	66.4 ± 1.1 (0)	–
−57.59	−295.2 ± 65.6	S	−8.696 ± 1.053	0.920 ± 0.061	73.0 ± 1.0 (+)	–
NGC 2787	−1.1	0.149 ± 0.024	7.524 ± 1.254	−22.40 ± 0.36	10.224 ± 0.145	210 ± 15
353.25	723.0 ± 10.0	29.422 ± 0.362	−0.891 ± 0.149	−19.13 ± 0.37	55.5 ± 1.6 (−)	194.3 ± 2.2
−7.67	309.0 ± 67.2	S	−1.021 ± 0.192	0.923 ± 0.054	109.0 ± 1.0 (−)	61.9 ± 1.5
NGC 2903	4.0	0.035 ± 0.006	5.492 ± 0.476	−23.99 ± 0.19	10.586 ± 0.076	188 ± 4
30.00	555.6 ± 1.3	29.733 ± 0.188	3.170 ± 0.275	−21.37 ± 0.20	61.2 ± 0.5 (−)	260.5 ± 0.7
−43.60	−173.0 ± 38.4	TF in I	−6.038 ± 0.535	0.546 ± 0.050	23.0 ± 1.0 (−)	2.2 ± 0.7
M81	2.4	0.091 ± 0.015	3.709 ± 0.147	−24.34 ± 0.09	10.905 ± 0.035	199 ± 11
355.97	−39.4 ± 2.8	27.867 ± 0.086	−0.262 ± 0.010	−21.66 ± 0.12	57.2 ± 1.8 (−)	141.3 ± 2.5
−4.89	−173.3 ± 11.2	C,P,S,T	−0.318 ± 0.018	0.795 ± 0.052	151.3 ± 1.1 (−)	57.3 ± 1.4
M82	3.0	0.181 ± 0.029	3.450 ± 0.229	−23.82 ± 0.25	10.573 ± 0.099	110 ± 5
355.59	199.0 ± 7.0	27.709 ± 0.144	−0.266 ± 0.018	−20.67 ± 0.25	76.0 ± 1.8 (−)	104.1 ± 2.0
−4.25	86.6 ± 15.2	T	−0.257 ± 0.026	0.625 ± 0.057	67.0 ± 3.0 (+)	−24.4 ± 2.9
NGC 3115	−2.9	0.053 ± 0.009	1.930 ± 0.099	−24.39 ± 0.11	11.016 ± 0.045	262 ± 9
73.88	663.0 ± 5.0	30.064 ± 0.111	6.678 ± 0.341	−21.43 ± 0.12	86.0 ± 0.5 (−)	133.6 ± 1.0
−47.06	−287.4 ± 25.4	P,S,T	−7.471 ± 0.388	0.917 ± 0.051	43.5 ± 1.0 (+)	29.7 ± 0.7
NGC 3344	4.0	0.037 ± 0.006	9.407 ± 0.672	−23.43 ± 0.16	10.356 ± 0.065	163 ± 4
37.43	586.8 ± 0.4	30.650 ± 0.155	7.200 ± 0.514	−20.90 ± 0.18	25.5 ± 0.5 (+)	38.8 ± 0.3
−28.07	−450.9 ± 59.5	TF in V	−6.318 ± 0.460	0.541 ± 0.050	156.1 ± 0.7 (−)	−3.1 ± 0.5
M95	3.0	0.032 ± 0.005	5.368 ± 0.109	−23.66 ± 0.06	10.589 ± 0.023	197 ± 9
51.68	772.0 ± 3.0	30.086 ± 0.044	6.791 ± 0.138	−20.71 ± 0.06	45.0 ± 2.0 (−)	249.6 ± 4.7
−33.11	−104.8 ± 13.2	C,P,T	−5.644 ± 0.117	0.733 ± 0.100	6.0 ± 7.0 (−)	−7.9 ± 2.6
M96	1.8	0.028 ± 0.005	5.283 ± 0.333	−23.97 ± 0.14	10.717 ± 0.056	224 ± 41
51.82	910.0 ± 9.0	30.041 ± 0.137	6.717 ± 0.424	−21.16 ± 0.15	49.5 ± 1.6 (+)	114.3 ± 4.7
−32.40	49.6 ± 38.8	C,P,S	−5.424 ± 0.350	0.736 ± 0.070	135.0 ± 5.0 (+)	−68.2 ± 3.7
NGC 3377	−4.8	0.039 ± 0.006	5.901 ± 0.353	−22.92 ± 0.13	10.355 ± 0.053	88 ± 7
49.49	690.0 ± 5.0	30.151 ± 0.130	6.908 ± 0.414	−20.00 ± 0.22	90.0 ± 10.0 (0)	305.1 ± 9.0
−31.47	−198.6 ± 38.9	P,S	−5.562 ± 0.341	0.820 ± 0.050	43.7 ± 2.4 (−)	−21.6 ± 6.0
M105	−4.8	0.027 ± 0.004	5.440 ± 0.183	−23.99 ± 0.08	10.862 ± 0.030	56 ± 2
51.07	916.0 ± 5.0	30.057 ± 0.073	6.734 ± 0.226	−20.85 ± 0.10	90.0 ± 10.0 (0)	320.9 ± 8.5
−31.91	53.8 ± 21.3	P,S	−5.390 ± 0.186	0.928 ± 0.050	70.0 ± 2.1 (−)	−0.3 ± 5.6
NGC 3384	−2.7	0.031 ± 0.005	5.868 ± 0.327	−23.67 ± 0.12	10.712 ± 0.049	108 ± 28
51.06	737.0 ± 5.0	30.218 ± 0.121	7.261 ± 0.405	−20.29 ± 0.14	62.8 ± 1.6 (0)	–
−31.83	−181.5 ± 37.1	P,S,T	−5.795 ± 0.330	0.896 ± 0.050	50.5 ± 2.5 (−)	–
NGC 3412	−2.0	0.032 ± 0.005	6.113 ± 0.363	−22.79 ± 0.13	10.344 ± 0.052	121 ± 11
50.44	850.0 ± 2.0	30.258 ± 0.129	7.400 ± 0.440	−19.83 ± 0.20	57.0 ± 1.6 (0)	–
−30.97	−79.1 ± 40.5	S	−5.761 ± 0.350	0.874 ± 0.050	151.0 ± 0.9 (+)	–
NGC 3489	−1.3	0.019 ± 0.003	6.619 ± 0.439	−23.22 ± 0.14	10.468 ± 0.058	97 ± 12
50.79	702.0 ± 5.0	30.395 ± 0.144	8.112 ± 0.538	−20.22 ± 0.18	58.5 ± 3.0 (−)	169.4 ± 2.8
−28.67	−275.0 ± 49.5	S	−5.726 ± 0.388	0.807 ± 0.050	72.1 ± 0.9 (+)	13.8 ± 1.5
NGC 3621	6.9	0.091 ± 0.015	−1.628 ± 0.051	−22.99 ± 0.08	10.093 ± 0.031	140 ± 4
105.02	728.5 ± 2.7	29.283 ± 0.068	6.066 ± 0.190	−20.41 ± 0.08	64.4 ± 0.5 (+)	79.1 ± 2.0
−28.20	−44.8 ± 12.8	C,T	−3.368 ± 0.110	0.422 ± 0.052	163.3 ± 2.1 (−)	30.3 ± 0.9
M66	3.0	0.036 ± 0.006	5.593 ± 0.010	−24.50 ± 0.02	10.809 ± 0.007	199 ± 11
53.43	708.2 ± 1.1	30.074 ± 0.004	7.539 ± 0.014	−21.79 ± 0.04	63.4 ± 1.6 (−)	244.5 ± 0.7
−24.23	−148.4 ± 4.5	C,P	−4.224 ± 0.008	0.575 ± 0.050	173.0 ± 0.5 (+)	−37.7 ± 1.6
NGC 4144	6.0	0.017 ± 0.003	6.739 ± 0.090	−20.19 ± 0.05	8.991 ± 0.022	74 ± 5
24.07	265.0 ± 1.0	29.346 ± 0.029	3.011 ± 0.040	−18.00 ± 0.18	79.0 ± 1.4 (−)	283.7 ± 1.6
−3.06	−210.1 ± 8.2	T	−0.395 ± 0.007	0.447 ± 0.100	102.0 ± 0.5 (−)	30.1 ± 0.5

Table 1 – *continued*

Galaxy $L_{\rm sheet}$ $B_{\rm sheet}$ (1)	T $V_\odot$ $V_{\rm LG}$ (2)	τ_1 DM Method (3)	$X_{\rm sheet}$ $Y_{\rm sheet}$ $Z_{\rm sheet}$ (4)	M_{Ks} M_V $B-V$ (5)	$\log \mathcal{M}_{\rm stars}$ i PA (6)	$V_{\rm flat}$ $L_{\rm sheet}(AM)$ $B_{\rm sheet}(AM)$ (7)
NGC 4236	7.9	0.017 ± 0.003	4.393 ± 0.486	−20.91 ± 0.33	9.182 ± 0.133	85 ± 5
2.38	−10.0 ± 5.0	28.220 ± 0.240	0.182 ± 0.020	−18.68 ± 0.25	76.2 ± 0.5 (−)	154.3 ± 8.4
5.35	−174.4 ± 25.2	T	0.412 ± 0.031	0.312 ± 0.050	158.1 ± 2.0 (+)	−78.6 ± 1.0
NGC 4244	6.1	0.024 ± 0.004	3.626 ± 0.062	−21.40 ± 0.48	9.410 ± 0.191	99 ± 2
32.78	244.0 ± 2.0	28.183 ± 0.037	2.335 ± 0.040	−19.10 ± 0.42	84.5 ± 0.5 (+)	306.1 ± 0.6
−3.53	−47.2 ± 7.1	T	−0.266 ± 0.007	0.356 ± 0.050	43.6 ± 1.4 (−)	−30.8 ± 1.4
M106	4.0	0.018 ± 0.003	6.953 ± 0.291	−24.28 ± 0.09	10.701 ± 0.037	205 ± 9
23.71	450.0 ± 1.0	29.404 ± 0.091	3.054 ± 0.128	−21.71 ± 0.10	66.9 ± 0.9 (−)	235.4 ± 1.5
−1.37	−32.6 ± 20.6	C,P,S,T	−0.182 ± 0.013	0.549 ± 0.050	150.0 ± 0.5 (−)	65.3 ± 0.7
NGC 4449	9.8	0.022 ± 0.003	3.609 ± 0.070	−21.00 ± 0.06	9.280 ± 0.023	75 ± 9
27.24	214.0 ± 6.0	28.043 ± 0.042	1.858 ± 0.036	−18.45 ± 0.19	56.3 ± 2.6 (−)	261.7 ± 2.9
0.18	−25.6 ± 8.9	T	0.013 ± 0.002	0.399 ± 0.100	57.0 ± 7.0 (−)	−14.4 ± 5.7
M104	1.1	0.058 ± 0.009	1.161 ± 0.081	−25.10 ± 0.15	11.303 ± 0.061	353 ± 10
82.75	1100.0 ± 3.0	29.852 ± 0.151	9.126 ± 0.635	−22.35 ± 0.19	84.8 ± 0.6 (+)	168.9 ± 0.6
−9.20	260.0 ± 34.5	P,S	−1.491 ± 0.113	0.920 ± 0.051	89.9 ± 0.3 (+)	−8.0 ± 0.3
NGC 4631	6.6	0.019 ± 0.003	5.833 ± 0.099	-23.43 ± 0.04	10.190 ± 0.018	145 ± 5
39.11	617.0 ± 10.0	29.381 ± 0.037	4.742 ± 0.081	−21.21 ± 0.05	85.1 ± 0.5 (+)	124.1 ± 0.6
−0.63	85.3 ± 14.0	T	−0.082 ± 0.004	0.310 ± 0.030	74.6 ± 11.4 (+)	3.3 ± 11.3
M94	2.4	0.020 ± 0.003	3.862 ± 0.096	−23.39 ± 0.06	10.458 ± 0.023	135 ± 21
31.04	306.7 ± 3.7	28.271 ± 0.054	2.325 ± 0.058	−20.17 ± 0.07	40.5 ± 0.9 (+)	354.6 ± 1.6
3.43	31.9 ± 9.4	P,T	0.270 ± 0.004	0.703 ± 0.050	111.3 ± 4.8 (−)	21.5 ± 2.9
M64	2.4	0.047 ± 0.007	3.179 ± 0.078	−23.43 ± 0.06	10.496 ± 0.022	164 ± 7
50.39	407.4 ± 7.0	28.489 ± 0.053	3.842 ± 0.094	−20.37 ± 0.08	56.4 ± 1.4 (+)	359.2 ± 1.4
0.99	18.1 ± 11.7	T	0.086 ± 0.001	0.734 ± 0.050	113.5 ± 0.5 (−)	27.1 ± 0.6
NGC 4945	6.1	0.201 ± 0.032	−1.720 ± 0.045	−23.70 ± 0.06	10.528 ± 0.024	174 ± 7
121.43	561.0 ± 3.0	27.614 ± 0.057	2.814 ± 0.074	−20.97 ± 0.22	81.7 ± 2.2 (+)	193.5 ± 2.8
−6.08	84.4 ± 11.5	T	−0.351 ± 0.013	0.629 ± 0.032	43.5 ± 1.5 (+)	39.5 ± 1.6
NGC 5023	5.9	0.020 ± 0.003	5.752 ± 0.098	−19.67 ± 0.07	8.736 ± 0.027	83 ± 2
28.75	406.0 ± 1.0	29.097 ± 0.037	3.156 ± 0.054	−17.54 ± 0.13	87.0 ± 2.0 (0)	–
7.23	3.7 ± 8.6	T	0.832 ± 0.012	0.381 ± 0.050	28.0 ± 0.5 (+)	–
NGC 5068	6.0	0.116 ± 0.019	−0.312 ± 0.013	−21.27 ± 0.10	9.501 ± 0.041	94 ± 9
93.44	668.0 ± 3.0	28.586 ± 0.091	5.202 ± 0.218	−18.97 ± 0.20	28.6 ± 1.2 (−)	–
−0.64	118.6 ± 13.9	P	−0.058 ± 0.008	0.550 ± 0.053	104.0 ± 1.0 (0)	–
NGC 5102	−3.0	0.062 ± 0.010	−1.000 ± 0.095	−20.74 ± 0.21	9.370 ± 0.084	95 ± 2
108.96	470.0 ± 5.0	27.445 ± 0.206	2.910 ± 0.276	−18.09 ± 0.29	70.0 ± 2.0 (+)	172.7 ± 2.5
−1.40	37.7 ± 19.9	P,T	−0.075 ± 0.019	0.661 ± 0.051	46.1 ± 3.1 (+)	31.4 ± 2.9
Centaurus A	−5.0	0.131 ± 0.021	−1.518 ± 0.007	−24.95 ± 0.25	11.169 ± 0.099	77 ± 7
115.40	541.0 ± 7.0	27.750 ± 0.010	3.197 ± 0.015	−21.92 ± 0.12	79.0 ± 10.0 (−)	14.3 ± 10.0
−2.02	66.1 ± 11.4	C,P,T	−0.125 ± 0.001	0.820 ± 0.021	80.0 ± 5.0 (−)	−0.6 ± 5.0
M51	4.0	0.040 ± 0.006	7.129 ± 0.348	−24.24 ± 0.11	10.647 ± 0.044	224 ± 58
25.86	464.0 ± 3.0	29.524 ± 0.106	3.455 ± 0.169	−21.30 ± 0.12	20.0 ± 5.0 (−)	202.8 ± 1.9
10.38	−20.2 ± 23.9	P	1.451 ± 0.065	0.492 ± 0.012	169.0 ± 4.2 (+)	−29.3 ± 4.9
NGC 5195	−1.0	0.041 ± 0.007	6.746 ± 0.820	−23.36 ± 0.27	10.524 ± 0.106	105 ± 11
25.79	601.0 ± 8.5	29.403 ± 0.264	3.259 ± 0.396	−19.89 ± 0.27	42.5 ± 1.8 (+)	342.6 ± 1.9
10.46	148.3 ± 55.3	S	1.383 ± 0.152	0.809 ± 0.012	94.5 ± 3.5 (−)	12.1 ± 2.4
M83	5.0	0.075 ± 0.012	−1.096 ± 0.052	−24.08 ± 0.11	10.642 ± 0.042	172 ± 32
102.83	515.0 ± 1.0	28.467 ± 0.103	4.813 ± 0.228	−21.15 ± 0.12	25.0 ± 5.0 (+)	81.6 ± 4.4
1.95	−26.5 ± 15.7	C,P,T	0.168 ± 0.002	0.577 ± 0.032	46.0 ± 1.0 (−)	−13.0 ± 2.6
M101	5.9	0.010 ± 0.002	6.811 ± 0.408	−24.05 ± 0.14	10.494 ± 0.056	202 ± 33
18.50	244.0 ± 1.0	29.353 ± 0.130	2.278 ± 0.136	−21.48 ± 0.20	21.0 ± 3.0 (−)	186.0 ± 1.8
15.63	−156.2 ± 23.6	C,P,T	2.009 ± 0.113	0.390 ± 0.010	42.0 ± 2.0 (+)	2.3 ± 2.5
Circinus	3.3	0.649 ± 0.050	−3.193 ± 0.551	−23.68 ± 0.38	10.559 ± 0.150	154 ± 13
138.65	441.5 ± 1.5	28.145 ± 0.375	2.809 ± 0.485	−20.69 ± 0.41	69.9 ± 2.7 (−)	20.5 ± 4.2
−0.51	−86.6 ± 52.8	TF in V	−0.038 ± 0.029	0.681 ± 0.110	30.1 ± 6.1 (−)	−38.8 ± 5.4

Table 1 – *continued*

Galaxy $L_{\rm sheet}$ $B_{\rm sheet}$ (1)	T $V_\odot$ $V_{\rm LG}$ (2)	τ_1 DM Method (3)	$X_{\rm sheet}$ $Y_{\rm sheet}$ $Z_{\rm sheet}$ (4)	M_{Ks} M_V $B-V$ (5)	$\log \mathcal{M}_{\rm stars}$ i PA (6)	$V_{\rm flat}$ $L_{\rm sheet}(AM)$ $B_{\rm sheet}(AM)$ (7)
E274−G001	6.6	0.293 ± 0.047	−1.757 ± 0.042	−20.59 ± 0.29	9.235 ± 0.116	77 ± 3
125.07	522.0 ± 2.0	27.482 ± 0.052	2.502 ± 0.060	−17.97 ± 0.19	83.9 ± 2.6 (+)	213.0 ± 2.8
15.17	128.1 ± 11.2	T	0.829 ± 0.017	0.561 ± 0.066	43.1 ± 1.0 (+)	19.2 ± 1.1
Milky Way	3.0	0.000 ± 0.000	−0.004 ± 0.000	−25.26 ± 0.29	11.095 ± 0.118	226 ± 11
134.09	−11.1 ± 1.2	14.593 ± 0.042	0.004 ± 0.000	−22.12 ± 0.20	90.0 ± 0.0 (+)	224.8 ± 0.0
87.57	−46.5 ± 9.0	–	0.135 ± 0.000	0.551 ± 0.051	31.7 ± 0.0 (+)	0.7 ± 0.0
NGC 6503	5.9	0.036 ± 0.006	4.500 ± 0.441	−21.57 ± 0.21	9.635 ± 0.086	116 ± 1
350.36	25.5 ± 0.4	28.559 ± 0.213	−0.765 ± 0.075	−18.95 ± 0.22	72.7 ± 1.1 (−)	260.2 ± 1.4
28.83	−106.4 ± 23.3	T	2.513 ± 0.234	0.569 ± 0.030	120.8 ± 0.5 (−)	−39.8 ± 0.6
NGC 6946	5.9	0.390 ± 0.062	4.269 ± 0.433	−23.92 ± 0.22	10.529 ± 0.089	200 ± 23
329.99	43.7 ± 3.3	28.947 ± 0.220	−2.466 ± 0.250	−21.59 ± 0.29	32.6 ± 1.0 (+)	355.0 ± 1.5
37.75	−121.2 ± 32.3	P	3.817 ± 0.374	0.506 ± 0.115	65.9 ± 3.2 (−)	13.1 ± 1.3
IC 5052	7.1	0.058 ± 0.009	−5.736 ± 0.098	−21.12 ± 0.30	9.366 ± 0.120	87 ± 4
171.09	584.0 ± 3.0	28.851 ± 0.037	0.900 ± 0.015	−18.68 ± 0.21	85.7 ± 3.2 (+)	88.3 ± 3.3
11.00	26.1 ± 10.2	T	1.128 ± 0.017	0.448 ± 0.051	140.0 ± 1.0 (+)	−14.9 ± 1.2
NGC 7793	7.4	0.022 ± 0.003	−2.995 ± 0.332	−21.27 ± 0.25	9.448 ± 0.099	112 ± 8
216.62	226.2 ± 1.2	27.897 ± 0.241	−2.226 ± 0.247	−18.94 ± 0.26	51.7 ± 2.1 (−)	344.9 ± 2.2
12.50	−33.1 ± 29.8	T	0.827 ± 0.078	0.477 ± 0.020	104.7 ± 5.4 (−)	−3.8 ± 4.2

(1) Name of galaxy, in order of right ascension; Longitude in rotated Sheet coordinates, in degrees; Latitude in rotated Sheet coordinates, in degrees. The natural Sheet coordinate system has its north pole (the direction of positive z) at supergalactic coordinates $(L, B) = (241\overset{\circ}{.}74 \pm 0\overset{\circ}{.}74, 82\overset{\circ}{.}05 \pm 0\overset{\circ}{.}12)$ with the x–y plane perpendicularly offset from the Sun southward of the supergalactic plane by 129 ± 4 kpc. The positive x-axis points parallel to the line of nodes towards $L = 151\overset{\circ}{.}74$ and the positive y-axis points towards the supergalactic longitude of the north pole. In the rotated system, the x-axis has been rotated by $106\overset{\circ}{.}74$ clockwise, so longitudes of galaxies are concomitantly greater. (2) Numerical index of the morphological stage in the Revised Hubble System; Heliocentric radial velocity, in km s^{-1}; Radial velocity, corrected for the Hubble flow if the heliocentric distance is beyond 1 Mpc, in the frame of reference of the luminosity-weighted centroid of the Local Group, in km s^{-1}. The value adopted for the Hubble constant was 71.6 km s^{-1} Mpc^{-1}. (3) Optical depth of interstellar dust in the Milky Way at 1 μm; Heliocentric distance modulus on the maser scale (Humphreys et al. 2013), in mag; Method used to determine the distance modulus (C = Cepheid variables in V and I; FP = Fundamental Plane; P = planetary nebulae; S = surface brightness fluctuations in I; T = tip of the red giant branch in I; TF = Tully–Fisher relation). The distance to the centre of the Milky Way is from van der Marel et al. (2012). For any distance determined using more than one method, the tabulated error is the standard deviation of the estimates. Otherwise, the error comes from propagating uncertainties in observational parameters. The uncertainty in the zero-point of the distance scale is not included. Even though M106 (NGC 4258) sets the zero-point via its masers, the uncertainty recorded for its distance is based upon the dispersion of its stellar indicators. (4) Rotated Cartesian Sheet coordinates, in Mpc. The origin is the projection of the Sun on to the plane of the Local Sheet. In this system, the luminosity-weighted centroid of the Local Group is at $(X, Y, Z) = (0.124, -0.297, 0.200)$, and the centre of the Council of Giants is at $(X, Y, Z) = (0.362, 0.718, 0.000)$. (5) Absolute magnitude in K_s, in mag; Absolute magnitude in V, in mag; Fully corrected integrated $B-V$ colour, in mag. (6) Logarithm of the stellar mass, in solar units, based upon an absolute magnitude for the Sun of 3.315 mag in K_s (the uncertainty accounts only for the error in the luminosity); Inclination to the plane of the sky, in degrees; Position angle of the line of nodes, measured in degrees eastward from north to the first limb (epoch 1950 assumed). Symbols in parentheses next to the inclination and position angle resolve the ambiguity in the orientation of the spin vector. In the case of the inclination, the symbol + (−) signifies arms open counter-clockwise (clockwise) or that the near side is at the position angle of the receding limb plus (minus) 90°. In the case of the position angle, the symbol signifies whether the specified limb is receding (+) or approaching (−). The symbol 0 signifies indeterminate. (7) Tilt-corrected rotational velocity in the plateau of the rotation curve, in km s^{-1}; Longitude of the angular momentum vector in rotated Sheet coordinates, in degrees; Latitude of the angular momentum vector in rotated Sheet coordinates, in degrees.

A critical assessment of photometric and kinematic determinations was made for each galaxy, and an appropriate value of the tilt of the optically visible extent was adopted after taking into account such factors as passband, spatial coverage, obscuration, morphology, distortions, interactions, and the tilt itself. Generally, an isophotal tilt was preferred for galaxies viewed close to edge-on (tilt >80° – see Verheijen & Sancisi 2001), and a kinematic value was preferred for galaxies close to face-on (tilt <30°). In between, usually an average was adopted, in which case the uncertainty was taken to be half of the difference between the preferred photometric and kinematic values. Major axis position angles were similarly estimated from optical photometry and velocity fields, but with no restrictions on kinematic measurements. Photometric and kinematic estimates of orientations are summarized in Table 3, and adopted values are summarized in both Tables 1 and 3. Sources of observations are provided in Table 2.

Depending upon tilt, there are two or four possible orientations of the angular momentum vector for any given axis ratio and position angle. For each disc galaxy, the ambiguity was broken by identifying the direction of rotation of the limb specified by the position angle of the line of nodes as well as the top or near side from the handedness of the winding of the spiral arms or, for a few highly inclined systems, the pattern of obscuration (Kapranidis & Sullivan 1983). For a few predominantly spheroidal systems, the orientation of the angular momentum vector for the main body could be established from the kinematics of old stellar components [planetary

Table 2. Sources of observations.

Galaxy (1)	Velocity (2)	Orientation (3)	Rotation (4)	Photometry (5)	Distance (6)
NGC 55	puc91	kis88, pat03, puc91	puc91	pat03, fit90, jar03	gie08, set05
Andromeda	mar12, got70	sak00, pie92, vau58, got70	car06	wal87, jar03	fre01, cia89b, fer00, ton01, dur01, mcc05
NGC 247	car90	car85, car90, hla11	car90	car85, pat03, jar03	kar06, mou08
NGC 253	pen81, sco85	pen80, pen81	sof97	pen80, fit90, jar03	rek05, kar03c, mou05
NGC 300	puc90, rog79	car85, puc90	puc90	car85, pat03, jar03	fre01, sof96, riz07, sak04, but04
M33	new80a	sak00, pie92, vau59, new80a	new80a	pie92, vau59, jar03	fre01, cia04, riz07, kim02, gal04, mcc04, mcc05
M74	sho84, kam92	mol04, sho84, kam92	TF in K_s	pat03, mar01, jar03	her08
NGC 672	gar03	her96, gar03	gar03	pat03, her96, jar03	her96, gar03
NGC 891	oo07, swa97	sof93, mar01, oos07	san79, sof97	pat03, jar03	cia91, mou08
NGC 925	blo08	sak00, pis00, blo08	blo08	pat03, mac00, jar03	fre01
NGC 1023	noo08	noo08	noo08, agu03	bar75, pat03, jar03	cia91, ton01
Maffei 1	fin03	but99	–	but99, jar03	but99, fin03
Maffei 2	hur96, but99	but99, hur96	hur96, fin07	but99, jar03	but99, hur96, fin07
Dwingeloo 1	bur96, but99	but99, bur96	bur96	but99, jar03, twins N0598 and N0925	but99, bur96
NGC 1313	ryd95	ryd95, mar82	ryd95	pat03, ryd95, jar03	riz07
IC 342	new80b	but99, new80b	sof97, new80b	but99, jar03	sah02, her08, fin07
NGC 1569	sti02	but99	sti02	hun06, but99, vad05	gro08
NGC 2403	fra02	sak00, pie92, pat03, fra02	fra02	pie92, oka77, jar03	fre01, cia02
NGC 2683	cas91	her96, cas91	cas91	pat03, her96, jar03	ton01
NGC 2784	bla01	kir08	dre83	pat03, jar03	ton01
NGC 2787	ber95	nei99, erw03	erw03	pat03, fis08, jar03	ton01
NGC 2903	blo08	fis08, her96, her05	blo08	pat03, her96, fis08, jar03	her96, blo08
M81	blo08	but99, fis08, mol04, blo08	blo08, adl96	pat03, but99, fis08, jar03	fre01, jac89, ton01, riz07, sak04
M82	ach95	may05, ach95	ach95	pat03, ich95	sak99
NGC 3115	cap93, nor06	cap87, ems99	cap93	pat03, str77, jar03	cia02, ton01, els97
NGC 3344	ver00	ver00	ver00	pat03, jar03	pat03, ver00
M95	but88	sak00, her96, but88	but88	mac00, jar03	fre01, cia02, riz07, sak04
M96	her99	sak00, moi04	her99, veg01	mac00, jar03	fre01, fel97, ton01
NGC 3377	ems04	pat03, cap07, cop04	sim02, cop04	pat03, jar03	cia89a, ton01
M105	ems04	cap90, cap07, geb00	sta99	cap90, pat03, jar03	cia89a, ton01
NGC 3384	ems04	bus96, cap07	zee02	bus96, pat03, jar03	cia89a, ton01, mou09
NGC 3412	agu03	agu03	agu03	pat03, jar03	ton01
NGC 3489	ems04	nei99, cap07	cao00	pat03, jar03	ton01
NGC 3621	blo08	sak00, pat03, blo08	blo08	mac00, jar03	fre01, riz07, sak04
M66	blo08	sak00, fis08, pat03, blo08	blo08	mac00, jar03	fre01, cia02
NGC 4144	gar02	swa02, gar02	gar02	mak99, jar03	set05
NGC 4236	sho73	swa02, dai06	sho73	pie92, pat03, jar03	kar02a
NGC 4244	dah05	fry99, pat03, oll96, dah05	oll96	pat03, jar03	kar03a, set05
M106	alb80, wev86	fis08, pat03, alb80, wev86	alb80	pat03, fis08, jar03	mac06, cia02, ton01, riz07, mac06
NGC 4449	hun98	hun99, hun98	hun98	mak99, jar03	ann08, kar03a
M104	baj84	bur86, hou61, sch78	baj84, rub85	bur86, pat03, jar03	for96, ton01
NGC 4631	ran94	hum90, pat03, ran94	ran94	hum90, jar03	set05
M94	blo08	mol04, fis08, blo08	blo08	pat03, fis08, jar03	her08, kar03a
M64	blo08	fis08, her96, blo08	rix95	pat03, fis08, jar03	mou08
NGC 4945	dah93, ott01	vau64, dah93, ott01	sof97	pat03, jar03, twins N3877 and N4157	mou08, mou05
NGC 5023	gar02	swa02, bot86, gar02	gar02	pat03, jar03	set05
NGC 5068	kor04	ryd94, hel04	kor04	pat03, jar03	her08
NGC 5102	woe93	pat03, woe93	woe93	pat03, jar03	mcm94, kar02b
Centaurus A	hui95	hui95, duf79, wil86, woo07	woo07	duf79, jar03	fer07, hui93, riz07, rej05, har99, sor96
M51	tul74, til91	fis08, pat03, tul74, dai06, kun97	dai06, kun97	oka76, fis08, jar03	fel97
NGC 5195	sch77	bri01, sch77, spi92	sch77	oka76, jar03	ton01
M83	cro02	pat03, hel04, cro02	cro02	tal79, jar03	thi03, her08, kar07
M101	won04	won04, her05	won04	oka76, jar03	fre01, fel97, riz07, sak04
Circinus	jon99, cur08	fre77, cur08, pat03	cur08, jon99	fre77, jar03	fre77, cur08, jon99
E274-G001	kor04	pat03	kor04	pat03, jar03	kar07
Milky Way	mar12	defined	car06, xue08, sof09, rei09, mcm11, mar12	TF in V, TF in K_s, twin N0891	mar12
NGC 6503	beg87	her96, beg87	beg87	mak99, vau82, jar03	kar03b
NGC 6946	blo08	abl71, blo08	blo08	mak99, fis08, jar03	her08

Table 2 – *continued*

Galaxy (1)	Velocity (2)	Orientation (3)	Rotation (4)	Photometry (5)	Distance (6)
IC 5052	kor04	kir08	kor04	pat03, jar03	set05
NGC 7793	blo08	car85, blo08	blo08	car85, vau80, jar03	kar03c

(1) Name of galaxy, in order of right ascension. (2) Origin of heliocentric velocity. (3) Origin of axis ratio, tilt, and position angle. (4) Origin of velocity field. (5) Origin of integrated photometry ($B - V$, V, and K_s). (6) Origin of observations required to determine distance.

Translations: abl71 (Ables 1971); ach95 (Achtermann & Lacy 1995); adl96 (Adler & Westpfahl 1996); agu03 (Aguerri, Debattista & Corsini 2003); alb80 (van Albada 1980); ann08 (Annibali et al. 2008); baj84 (Bajaja et al. 1984); bar75 (Barbon & Capaccioli 1975); beg87 (Begeman 1987); ber95 (Bertola et al. 1995); bla01 (Blakeslee et al. 2001); blo08 (de Blok et al. 2008); bot86 (Bottema, Shostak & van der Kruit 1986); bri01 (Bridzius & Vansevicius 2001); bur86 (Burkhead 1986); bur96 (Burton et al. 1996); bus96 (Busarello et al. 1996); but88 (Buta 1988); but99 (Buta & McCall 1999); but04 (Butler, Martínez-Delgado & Brandner 2004); cao00 (Caon, Macchetto & Pastoriza 2000); cap87 (Capaccioli, Held & Nieto 1987); cap90 (Capaccioli et al. 1990); cap93 (Capaccioli et al. 1993); cap07 (Cappellari et al. 2007); car85 (Carignan 1985); car90 (Carignan & Puche 1990); car06 (Carignan et al. 2006); cas91 (Casertano & van Gorkom 1991); cia89a (Ciardullo et al. 1989a); cia89b (Ciardullo, Jacoby & Ford 1989b); cia91 (Ciardullo, Jacoby & Harris 1991); cia02 (Ciardullo et al. 2002); cia04 (Ciardullo et al. 2004); cop04 (Copin, Cretton & Emsellem 2004); cro02 (Crosthwaite et al. 2002); cur08 (Curran et al. 2008); dah93 (Dahlem et al. 1993); dah05 (Dahlem et al. 2005); dai06 (Daigle et al. 2006); dre83 (Dressler & Sandage 1983); duf79 (Dufour et al. 1979); dur01 (Durrell, Harris & Pritchet 2001); els97 (Elson 1997); ems99 (Emsellem, Dejonghe & Bacon 1999); ems04 (Emsellem et al. 2004); erw03 (Erwin & Sparke 2003); fel97 (Feldmeier, Ciardullo & Jacoby 1997); fer00 (Ferrarese et al. 2000); fer07 (Ferrarese et al. 2007); fin03 (Fingerhut et al. 2003); fin07 (Fingerhut et al. 2007); fis08 (Fisher & Drory 2008); fit90 (Fitzgibbons 1990); for96 (Ford et al. 1996); fra02 (Fraternali et al. 2002); fre77 (Freeman et al. 1977); fre01 (Freedman et al. 2001); fry99 (Fry et al. 1999); gal04 (Galleti, Bellazzini & Ferraro 2004); gar02 (García-Ruiz, Sancisi & Kuijken 2002); gar03 (Garrido et al. 2003); geb00 (Gebhardt et al. 2000); gie08 (Gieren et al. 2008); got70 (Gottesman & Davies 1970); gro08 (Grocholski et al. 2008); har99 (Harris, Harris & Poole 1999); hel04 (Helmboldt et al. 2004); her96 (Heraudeau & Simien 1996); her99 (Héraudeau et al. 1999); her05 (Hernandez et al. 2005); her08 (Herrmann et al. 2008); hla11 (Hlavacek-Larrondo et al. 2011); hou61 (van Houten 1961); hui93 (Hui et al. 1993); hui95 (Hui et al. 1995); hum90 (Hummel & Dettmar 1990); hun98 (Hunter et al. 1998); hun99 (Hunter, van Woerden & Gallagher 1999); hun06 (Hunter & Elmegreen 2006); hur96 (Hurt, Turner & Ho 1996); ich95 (Ichikawa et al. 1995); jac89 (Jacoby et al. 1989); jar03 (Jarrett et al. 2003); jon99 (Jones et al. 1999); kam92 (Kamphuis & Briggs 1992); kar02a (Karachentsev et al. 2002a); kar02b (Karachentsev et al. 2002b); kar03a (Karachentsev et al. 2003a); kar03b (Karachentsev et al. 2003b); kar03c (Karachentsev et al. 2003); kar06 (Karachentsev et al. 2006); kar07 (Karachentsev et al. 2007); kim02 (Kim et al. 2002); kir08 (Kirby et al. 2008); kis88 (Kiszkurno-Koziej 1988); kor04 (Koribalski et al. 2004); kun97 (Kuno & Nakai 1997); mac00 (Macri et al. 2000); mac06 (Macri et al. 2006); mak99 (Makarova 1999); mar82 (Marcelin & Athanassoula 1982); mar01 (Marcum et al. 2001); mar12 (van der Marel et al. 2012); may05 (Mayya, Carrasco & Luna 2005); mcc04 (McConnachie et al. 2004); mcc05 (McConnachie et al. 2005); mcm94 (McMillan, Ciardullo & Jacoby 1994); mcm11 (McMillan 2011); moi04 (Moiseev, Valdés & Chavushyan 2004); mol04 (Möllenhoff 2004); mou05 (Mouhcine et al. 2005); mou08 (Mould & Sakai 2008); mou09 (Mould & Sakai 2009); nei99 (Neistein et al. 1999); new80a (Newton 1980a); new80b (Newton 1980b); noo08 (Noordermeer et al. 2008); nor06 (Norris, Sharples & Kuntschner 2006); oka76 (Okamura, Kanazawa & Kodaira 1976); oka77 (Okamura, Takase & Kodaira 1977); oll96 (Olling 1996); oos07 (Oosterloo, Fraternali & Sancisi 2007); ott01 (Ott et al. 2001); pat03 (Paturel et al. 2003); pen80 (Pence 1980); pen81 (Pence 1981); pie92 (Pierce & Tully 1992); pis00 (Pisano, Wilcots & Elmegreen 2000); puc90 (Puche, Carignan & Bosma 1990); puc91 (Puche, Carignan & Wainscoat 1991); ran94 (Rand 1994); rei09 (Reid et al. 2009); rej05 (Rejkuba et al. 2005); rek05 (Rekola et al. 2005); rix95 (Rix et al. 1995); riz07 (Rizzi et al. 2007); rog79 (Rogstad, Chu & Crutcher 1979); rub85 (Rubin et al. 1985); ryd94 (Ryder & Dopita 1994); ryd95 (Ryder et al. 1995); sah02 (Saha, Claver & Hoessel 2002); sak99 (Sakai & Madore 1999); sak00 (Sakai et al. 2000); sak04 (Sakai et al. 2004); san79 (Sancisi & Allen 1979); sch77 (Schweizer 1977); sch78 (Schweizer 1978); sco85 (Scoville et al. 1985); set05 (Seth, Dalcanton & de Jong 2005); sho73 (Shostak 1973); sho84 (Shostak & van der Kruit 1984); sim02 (Simien & Prugniel 2002); sof93 (Sofue & Nakai 1993); sof96 (Soffner et al. 1996); sof97 (Sofue 1997); sof09 (Sofue et al. 2009); sor96 (Soria et al. 1996); spi92 (Spillar et al. 1992); sta99 (Statler & Smecker-Hane 1999); sti02 (Stil & Israel 2002); str77 (Strom et al. 1977); swa97 (Swaters, Sancisi & van der Hulst 1997); swa02 (Swaters & Balcells 2002); tal79 (Talbot, Jensen & Dufour 1979); thi03 (Thim et al. 2003); til91 (Tilanus & Allen 1991); ton01 (Tonry et al. 2001); tul74 (Tully 1974); vad05 (Vaduvescu et al. 2005); vau58 (de Vaucouleurs 1958); vau59 (de Vaucouleurs 1959); vau64 (de Vaucouleurs 1964); vau80 (de Vaucouleurs & Davoust 1980); vau82 (de Vaucouleurs & Caulet 1982); veg01 (Vega Beltrán et al. 2001); ver00 (Verdes-Montenegro, Bosma & Athanassoula 2000); wal87 (Walterbos & Kennicutt 1987); wev86 (Wevers, van der Kruit & Allen 1986); wil86 (Wilkinson et al. 1986); woe93 (van Woerden et al. 1993); won04 (Wong, Blitz & Bosma 2004); woo07 (Woodley et al. 2007); xue08 (Xue et al. 2008); zee02 (de Zeeuw et al. 2002).

nebulae (PNe) in the case of Centaurus A: Wilkinson et al. 1986; Hui et al. 1995; Woodley et al. 2007]. Codes conveying the direction of rotation and the handedness of the spiral pattern (or the dustiest side of the disc) are provided in Table 1 next to the position angle and tilt, respectively.

The directions of the derived angular momentum vectors are given in Table 1 in a coordinate system anchored to the Sheet. With respect to positions mapped by Kapranidis & Sullivan (1983) for 20 galaxies in the sample (excluding NGC 247), the corresponding supergalactic positions differ on average by 11°. The largest discrepancies occur for galaxies which are heavily obscured and/or close to face-on. Results presented in this paper ought to be preferred because they benefit from more modern constraints on tilts and position angles. In the case of NGC 247, it appears that Kapranidis & Sullivan (1983) misidentified the receding side.

For some galaxies, tilted-ring models of H I velocity fields have enabled evaluation of disc orientations far beyond the extent of the stars. Generally, results are comparable to those found for optically visible matter. However, there are some galaxies for which the tilt appears to vary quite substantially with radius, indicative of a warp (e.g. the Circinus galaxy, for which the tilt drops from 66° to 47° over the radius range 10 to 25 arcmin: Curran, Koribalski & Bains 2008). For such objects, it is conceivable that the spin axis derived for the optical disc is not aligned with the spin axis of the dark matter halo, although it is also possible that an interaction has distorted the outer velocity field. Tilts and position angles presented in Table 1 and the angular momentum vectors which follow from them are quite homogeneously conveying the orientation of baryonic matter within the visible extent of the sample galaxies, but are not necessarily conveying the orientation of dark matter beyond. Note, however,

that for galaxies for which the radial variation of tilt has been mapped, the rotational velocity in the plateau of the rotation curve ($V_{\rm flat}$ in Table 1) was determined using a tilt appropriate for that radial domain.

3.3 Extinction

Any structure of which we are a part spans the entire sky, so obscuration by dust in the Milky Way varies drastically across it. Without accommodating for the effective wavelength shifts afflicting broad-

Table 3. Orientational data.

Galaxy (1)	*i* (phot) (2)	*i* (kin) (3)	*i* (4)	*PA* (phot) (5)	*PA* (kin) (6)	*PA* (7)	Notes (8)
NGC 55	81.2 ± 1.6	77.0 ± 2.0	81.2 ± 1.6	101.0 ± 1.0	109.0 ± 3.0	105.0 ± 4.0	1, 2
Andromeda	78.0 ± 2.6	78.0 ± 1.0	78.0 ± 0.5	37.7 ± 0.2	38.0 ± 1.0	37.9 ± 0.5	
NGC 247	75.5 ± 1.6	74.0 ± 1.0	74.8 ± 0.8	171.1 ± 0.1	170.0 ± 1.0	170.6 ± 0.5	
NGC 253	76.9 ± 1.7	75.0 ± 0.5	75.9 ± 0.9	51.0 ± 0.1	51.2 ± 0.8	51.1 ± 0.5	
NGC 300	42.7 ± 6.1	50.0 ± 3.0	46.4 ± 3.6	105.6 ± 1.8	108.0 ± 4.0	106.8 ± 1.2	
M33	54.0 ± 2.0	54.0 ± 1.0	54.0 ± 0.5	23.0 ± 1.0	22.0 ± 1.0	22.5 ± 0.5	
M74	14.2 ± 2.4	9.3 ± 0.9	9.3 ± 0.9	71.1 ± 1.0	25.0 ± 5.0	25.0 ± 5.0	3, 4
NGC 672	63.6 ± 0.8	65.0 ± 3.0	64.3 ± 0.7	71.0 ± 1.0	64.0 ± 3.0	67.5 ± 3.5	
NGC 891	88.3 ± 1.5	–	88.3 ± 1.5	22.0 ± 0.5	23.0 ± 1.0	22.5 ± 0.5	1
NGC 925	56.0 ± 1.1	66.0 ± 1.0	61.0 ± 5.0	112.0 ± 4.0	106.6 ± 1.0	109.3 ± 2.7	
NGC 1023	72.2 ± 1.3	–	72.2 ± 1.3	85.0 ± 1.0	–	85.0 ± 1.0	
Maffei 1	–	–	–	83.9 ± 0.7	–	83.9 ± 0.7	5, 6
Maffei 2	66.2 ± 0.6	67.0 ± 1.0	67.0 ± 1.0	23.0 ± 0.7	26.0 ± 1.0	24.5 ± 1.5	6
Dwingeloo 1	46.2 ± 0.3	51.0 ± 2.0	51.0 ± 2.0	110.7 ± 2.0	112.0 ± 1.0	111.4 ± 0.6	6
NGC 1313	42.7 ± 0.9	48.0 ± 3.0	45.4 ± 2.6	4.0 ± 10.0	1.0 ± 3.0	2.5 ± 1.5	
IC 342	29.5 ± 0.5	25.0 ± 3.0	25.0 ± 3.0	86.5 ± 1.6	39.0 ± 3.0	39.0 ± 3.0	6
NGC 1569	90.0 ± 1.0	–	90.0 ± 1.0	119.3 ± 1.1	–	119.3 ± 1.1	7
NGC 2403	58.0 ± 2.0	62.9 ± 2.1	60.5 ± 2.5	126.0 ± 1.0	124.5 ± 0.6	125.3 ± 0.8	
NGC 2683	79.3 ± 2.1	–	79.3 ± 2.1	44.0 ± 1.0	41.5 ± 1.0	42.8 ± 1.3	1
NGC 2784	66.4 ± 1.1	–	66.4 ± 1.1	73.0 ± 1.0	–	73.0 ± 1.0	5
NGC 2787	55.5 ± 1.6	–	55.5 ± 1.6	109.0 ± 1.0	–	109.0 ± 1.0	5
NGC 2903	60.9 ± 0.8	61.5 ± 0.5	61.2 ± 0.5	24.0 ± 1.0	22.0 ± 1.0	23.0 ± 1.0	
M81	55.5 ± 0.9	59.0 ± 1.0	57.2 ± 1.8	152.3 ± 1.0	150.2 ± 1.0	151.3 ± 1.1	
M82	76.0 ± 1.8	73.0 ± 3.0	76.0 ± 1.8	64.0 ± 1.0	70.0 ± 3.0	67.0 ± 3.0	8
NGC 3115	86.0 ± 5.2	86.0 ± 1.0	86.0 ± 0.5	43.5 ± 1.0	–	43.5 ± 1.0	
NGC 3344	25.3 ± 0.3	25.5 ± 0.5	25.5 ± 0.5	159.8 ± 1.6	156.1 ± 0.7	156.1 ± 0.7	3
M95	45.0 ± 2.0	–	45.0 ± 2.0	179.0 ± 1.0	13.0 ± 1.0	6.0 ± 7.0	7
M96	49.5 ± 1.6	–	49.5 ± 1.6	135.0 ± 5.0	–	135.0 ± 5.0	9
NGC 3377	–	90.0 ± 10.0	90.0 ± 10.0	41.3 ± 1.0	46.0 ± 1.0	43.7 ± 2.4	5
M105	–	90.0 ± 10.0	90.0 ± 10.0	67.9 ± 1.0	72.0 ± 2.0	70.0 ± 2.1	5
NGC 3384	62.8 ± 1.6	–	62.8 ± 1.6	53.0 ± 1.0	48.0 ± 1.5	50.5 ± 2.5	
NGC 3412	57.0 ± 1.6	–	57.0 ± 1.6	151.0 ± 0.9	–	151.0 ± 0.9	
NGC 3489	58.5 ± 3.0	–	58.5 ± 3.0	71.2 ± 1.0	73.0 ± 1.0	72.1 ± 0.9	
NGC 3621	64.0 ± 1.1	64.7 ± 1.0	64.4 ± 0.5	161.2 ± 1.0	165.4 ± 1.0	163.3 ± 2.1	
M66	65.0 ± 1.3	61.8 ± 1.0	63.4 ± 1.6	173.0 ± 1.0	173.0 ± 1.0	173.0 ± 0.5	
NGC 4144	79.0 ± 1.4	–	79.0 ± 1.4	102.0 ± 1.0	102.0 ± 1.0	102.0 ± 0.5	
NGC 4236	76.4 ± 1.2	76.1 ± 0.7	76.2 ± 0.5	160.0 ± 1.0	156.1 ± 1.6	158.1 ± 2.0	
NGC 4244	88.1 ± 6.9	84.5 ± 0.5	84.5 ± 0.5	42.2 ± 1.0	45.0 ± 2.0	43.6 ± 1.4	1, 5
M106	66.9 ± 0.9	72.0 ± 1.0	66.9 ± 0.9	150.0 ± 1.0	150.0 ± 1.0	150.0 ± 0.5	8
NGC 4449	56.3 ± 2.6	60.0 ± 5.0	56.3 ± 2.6	64.0 ± 1.0	50.0 ± 17.0	57.0 ± 7.0	7
M104	84.8 ± 0.6	–	84.8 ± 0.6	89.9 ± 0.3	–	89.9 ± 0.3	
NGC 4631	84.6 ± 2.6	85.5 ± 1.5	85.1 ± 0.5	63.3 ± 1.0	86.0 ± 1.0	74.6 ± 11.4	1, 5, 8
M94	39.7 ± 3.8	41.4 ± 1.0	40.5 ± 0.9	106.5 ± 1.0	116.1 ± 1.0	111.3 ± 4.8	10
M64	57.7 ± 0.9	55.0 ± 2.0	56.4 ± 1.4	114.0 ± 1.0	113.0 ± 2.0	113.5 ± 0.5	9
NGC 4945	81.7 ± 2.2	78.0 ± 1.0	81.7 ± 2.2	42.0 ± 1.0	45.0 ± 2.0	43.5 ± 1.5	1
NGC 5023	78.2 ± 1.3	87.0 ± 2.0	87.0 ± 2.0	28.0 ± 1.0	28.0 ± 1.0	28.0 ± 0.5	1, 5
NGC 5068	28.6 ± 1.2	–	28.6 ± 1.2	104.0 ± 1.0	–	104.0 ± 1.0	3
NGC 5102	70.6 ± 2.7	70.0 ± 2.0	70.0 ± 2.0	49.2 ± 1.0	43.0 ± 3.0	46.1 ± 3.1	5
Centaurus A	–	79.0 ± 10.0	79.0 ± 10.0	35.0 ± 3.0	80.0 ± 5.0	80.0 ± 5.0	11
M51	39.1 ± 3.7	20.0 ± 5.0	20.0 ± 5.0	163.0 ± 1.0	169.0 ± 4.2	169.0 ± 4.2	
NGC 5195	42.5 ± 1.8	–	42.5 ± 1.8	91.0 ± 5.0	98.0 ± 25.0	94.5 ± 3.5	
M83	11.1 ± 24.7	25.0 ± 5.0	25.0 ± 5.0	85.0 ± 1.0	46.0 ± 1.0	46.0 ± 1.0	3
M101	35.3 ± 3.0	21.0 ± 3.0	21.0 ± 3.0	43.0 ± 6.0	42.0 ± 2.0	42.0 ± 2.0	
Circinus	69.9 ± 2.7	66.0 ± 5.0	69.9 ± 2.7	36.1 ± 1.0	24.0 ± 3.0	30.1 ± 6.1	6, 8
E274-G001	83.9 ± 2.6	–	83.9 ± 2.6	43.1 ± 1.0	–	43.1 ± 1.0	
Milky Way	90.0 ± 0.0	90.0 ± 0.0	90.0 ± 0.0	31.7 ± 0.0	31.7 ± 0.0	31.7 ± 0.0	

Table 3 – *continued*

Galaxy (1)	*i* (phot) (2)	*i* (kin) (3)	*i* (4)	*PA* (phot) (5)	*PA* (kin) (6)	*PA* (7)	Notes (8)
NGC 6503	71.5 ± 0.9	73.8 ± 1.2	72.7 ± 1.1	121.0 ± 1.0	120.6 ± 0.9	120.8 ± 0.5	
NGC 6946	33.2 ± 1.1	32.6 ± 1.0	32.6 ± 1.0	69.0 ± 5.0	62.7 ± 1.0	65.9 ± 3.2	6
IC 5052	85.7 ± 3.2	–	85.7 ± 3.2	140.0 ± 1.0	–	140.0 ± 1.0	
NGC 7793	53.8 ± 1.5	49.6 ± 1.0	51.7 ± 2.1	99.3 ± 1.1	110.1 ± 1.0	104.7 ± 5.4	

(1) Name of galaxy, in order of right ascension. (2) Tilt from photometry, in degrees. (3) Tilt from kinematics, in degrees. (4) Adopted tilt, in degrees. (5) Position angle of line of nodes from photometry, in degrees measured eastward from north (epoch 1950 assumed). (6) Position angle of line of nodes from kinematics, in degrees measured eastward from north (epoch 1950 assumed). (7) Adopted position angle of line of nodes, in degrees measured eastward from north (epoch 1950 assumed). (8) Points of relevance.

Notes. (1) highly inclined; (2) tilt from relative scale heights of different populations; (3) near face-on; (4) tilt derived from Tully–Fisher relation in K_s; (5) intrinsic axis ratio uncertain; (6) heavy extinction; (7) complex velocity field; (8) disturbed or warped; (9) gas captured; (10) non-circular motions and isophotes; (11) properties are for PNe in spheroidal component.

band photometry, significant systematic errors in distances and luminosities can arise for targets heavily obscured by dust (McCall 2004), be they galaxies at low Galactic latitudes or even Cepheid variables inside galaxies at high Galactic latitudes. Corrections to the apparent colours and brightnesses of standard candles and of the galaxies themselves were evaluated using the York Extinction Solver (YES; McCall 2004). First, the optical depth at 1 μm was derived for a spectral energy distribution (SED) characteristic of the probe of reddening. Then, the extinction was evaluated using a SED characteristic of the target to be corrected. Motions of the probe and target were accommodated by shifting SEDs in wavelength by amounts consistent with heliocentric velocities. K-corrections for the targets were determined simultaneously with the extinction. For tilted spiral galaxies, the extra extinction over face-on due to internal dust was estimated self-consistently using an algorithm constructed from observations of colours as a function of tilt (McCall 2004).

Except for the LMC and SMC (which were employed in the calibration of standard candles), all extinction analyses, Galactic and extragalactic, were founded upon a monochromatic reddening law generated from the algorithm of Fitzpatrick (Fitzpatrick 1999). Through an appropriate choice of parameter, the law was tuned to deliver a ratio of total to selective extinction $A_V/E(B-V)$ equal to 3.07 for the SED of Vega upon integration over *B* and *V* passbands (McCall 2004). This value is appropriate for the diffuse component of the interstellar medium of the Milky Way (McCall & Armour 2000), of which most of the dust obscuring extragalactic targets should be a part, and similarly should be characteristic of internal extinction in other galaxies with discs like that of the Milky Way. For the LMC and SMC, corrections for obscuration by internal dust were accomplished using reddening laws directly measured for those environments (Gordon et al. 2003).

For galaxies situated 10° or more away from the Galactic plane, optical depths due to dust in the Milky Way were derived from an all-sky map of the $B-V$ colour excesses of elliptical galaxies (Schlegel, Finkbeiner & Davis 1998). Individual determinations of optical depth were made for the most heavily obscured galaxies using H II regions (Maffei 2 – Fingerhut et al. 2007; IC 342 – Fingerhut et al. 2007; Circinus – this paper, using Oliva, Marconi & Moorwood 1999), the Mg_2 index (Maffei 1 – Fingerhut et al. 2003, 2007), or colours of lightly obscured analogues (Dwingeloo 1 – this paper). More comprehensive discussions of the extinction analyses and their impact on distances and luminosities are provided elsewhere (McCall 2004; Fingerhut et al. 2007).

3.4 Near-infrared magnitudes

The Tully–Fisher relation for spirals and the Fundamental Plane for ellipticals suggest that relative total masses of bright galaxies can be judged from stellar masses. To be a reliable proxy for stellar mass, the luminosity of each galaxy was characterized in the infrared, where it is not very sensitive to the star formation rate. Corrections for obscuration by internal and external dust were minimized by focusing on 2.2 μm (K_s), the reddest infrared passband for which data were readily available for most galaxies in the sample.

For all but three galaxies, apparent magnitudes in K_s were derived from 2MASS observations (Jarrett et al. 2003; Skrutskie et al. 2006). Better measurements were available for NGC 1569 (Vaduvescu et al. 2005) and M82 (Ichikawa et al. 1995). The magnitude for the Milky Way was estimated indirectly from its rotational velocity using the Tully–Fisher relation in K_s for galaxies in the Ursa Major cluster, which was constructed self-consistently for this paper (Section 3.5.7). Apparent magnitudes in *B* and *V*, which were needed to correct K_s magnitudes for imperfections in 2MASS photometry, were preferentially adopted from modern digital imaging studies.

Magnitudes from 2MASS for galaxies with low surface brightnesses are known to be systematically too faint (Kirby et al. 2008), and even measurements for bright galaxies are compromised by the finite extrapolation radii. Furthermore, 2MASS magnitudes for objects spanning two or more survey strips or in crowded fields are suspect. This is evidenced by the large deviation of Andromeda from the Tully–Fisher relation in K_s. To flag and correct deficiencies in 2MASS measurements, the relationship between the fully corrected colours $(V-K_s)^0$ and $(B-V)^0$ for the Local Volume sample was compared with that for a set of reference galaxies with impeccable independent near-infrared photometry (Fig. 1). Since total magnitudes in *B* and *V* are generally more robust than those in 2MASS K_s, it was expected that flaws in the K_s magnitudes would be revealed as deviations in $(V-K_s)^0$ from the norm for $(B-V)^0$.

The fiducial colour–colour relation was established using deep near-infrared and optical observations of a reference sample of galaxies spanning the Hubble sequence with apparent sizes small compared to the imaging arrays (de Jong & van der Kruit 1994; Gavazzi et al. 2003; Eisenhardt et al. 2007). To minimize uncertainties arising from corrections for internal extinction, spirals were required to have tilts close to face-on ($b/a > 0.625$: see de Jong & van der Kruit 1994). As shown in Fig. 1, $(V-K_s)^0$ is linearly correlated with $(B-V)^0$ across the Hubble sequence.

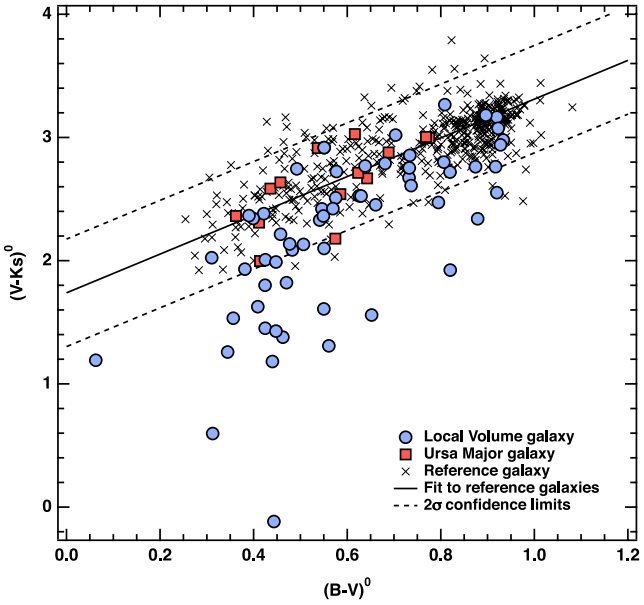

Figure 1. $(V - K_s)^0$ versus $(B - V)^0$ for galaxies across the Hubble sequence. Colours are corrected for Galactic extinction, internal extinction, and redshift. Galaxies in the reference sample, for which K_s magnitudes were measured independently from 2MASS, are identified with crosses. The fit and 2σ confidence limits are displayed as solid and dashed lines, respectively. Highly inclined galaxies in the Ursa Major cluster, which are marked by red squares, show precisely the same trend, verifying the integrity of internal extinction corrections. Galaxies in the Local Volume sample, for which K_s magnitudes were measured by 2MASS, are marked with blue circles. Near-infrared colours for Local Volume galaxies deviate blueward of the locus defined by the reference sample, showing that 2MASS magnitudes for them tend to be too faint.

Allowing for uncertainties in both coordinates, the line which best fits the reference sample is given by

$$(V - K_s)^0 = (1.739 \pm 0.054) + (1.572 \pm 0.071)(B - V)^0 \qquad (2)$$

with the vertical dispersion being only 0.22 mag. A collection of highly inclined spirals in the Ursa Major cluster (Verheijen & Sancisi 2001) displays precisely the same trend, verifying the reliability of the algorithm employed to correct disc galaxies for internal extinction.

Values of $(V - K_s)^0$ for Local Volume galaxies proved to be systematically shifted blueward of expectations by 0.20 mag. Thus, all 2MASS K_s magnitudes were brightened accordingly. Even then, some galaxies remained as blueward 'dropouts' (by 2.3 mag in the case of Dwingeloo 1 – see Fig. 1), showing that their K_s magnitudes were still too faint. For the 15 galaxies showing $(V - K_s)^0$ straying blueward of the fiducial relation by more than 2σ, K_s magnitudes were additionally adjusted by an amount equal to the deviation. In other words, the K_s magnitude for each was derived from the V magnitude by using equation (2) to evaluate the $V - K_s$ colour expected for its observed $B - V$ colour.

3.5 Distances

3.5.1 Overview

Catalogued distances for nearby galaxies are compromised by inhomogeneous approaches to analyses and imperfect alignment of the zero-points of different indices (Fingerhut et al. 2007). To come to definitive conclusions about local structure, it is imperative that these problems be eliminated. Thus, distances (and, in turn, luminosities) for this paper were derived from first principles. Required foundational observational parameters for the galaxies and their constituents were extracted or measured from published data.

For distance determinations, preference was given to four techniques founded upon stellar constituents: (1) the period–luminosity (PL) relations for Cepheid variables in V and I; (2) the luminosity cut-off for planetary nebulae (PNe) in the light of [O III]λ5007; (3) the characteristic luminosity of fluctuations in surface brightness (SBF) in I; and (4) the luminosity of the tip of the red giant branch (TRGB) in I. For galaxies lacking measurements of stellar constituents, distances were determined from the Fundamental-Plane or the Tully–Fisher relation.

First, distance scales for stellar constituents were unified with the Cepheid scale. This was accomplished through pairwise comparison of distances to galaxies for which more than one technique could be applied. To this end, the Local Volume sample was augmented with *HST* Key Project Cepheid calibrators (Freedman et al. 2001) and several galaxies of low metallicity for which good distances were derivable from multiple techniques (LMC, NGC 3109, SMC, WLM). Finally, all scales were shifted equally to bring the mean distance of M106 (NGC 4258) into coincidence with its distance of 7.60 ± 0.23 Mpc derived from nuclear masers (Humphreys et al. 2013).

Cepheid PL relations in V and I were adopted to be those of LMC Cepheids as defined by the OGLE II project (Macri et al. 2006), but after appropriately correcting (via YES) the zero-points for a systematic error in the mean extinctions (Fingerhut et al. 2007). To avoid a bias in galaxy mass or metallicity, the evaluation of the slope of the metallicity dependence of Cepheid distances was based solely upon a comparison of uncorrected distances from Cepheids with distances from the TRGB, which was possible for 18 galaxies.

To bring zero-points for the other stellar indicators on to the Cepheid scale, and to solve for the dependence of the PNe luminosity cut-off on metallicity, an analysis was made of 127 independent distance estimates for 34 galaxies for which distances could be derived by more than one of the stellar methods. The difference in distance moduli for every distance pairing possible for every galaxy (a total of 73 pairs) was computed, and the sum of the squares was minimized. Distance moduli flagged as leading to differences exceeding 0.3 mag in absolute value (2σ for the final fit) were pinpointed and rejected.

After aligning scales, the unweighted mean of the four distance moduli for M106 (NGC 4258) came out to be 0.124 ± 0.112 mag below the geometrical value derived from nuclear masers (Humphreys et al. 2013). The uncertainty here accounts for the error in the mean stellar distance (0.091 mag) and the maser distance (0.066 mag). Zero-points for the stellar indicators were adjusted accordingly to deliver distance moduli on the maser scale. For the LMC, the resultant mean distance modulus was 18.47 ± 0.13.

Distances to 52 of the sample galaxies could be derived from one or more of the stellar techniques. Distances to galaxies for which more than one technique could be applied were computed by averaging unrejected moduli with no weighting. The distance to the centre of the Milky Way was adopted to be 8.29 ± 0.16 kpc based upon a modern synthesis of extant measurements (van der Marel et al. 2012). For the remaining seven galaxies, distances were derived from an updated version of the Fundamental Plane for ellipticals in I (Maffei 1) or new constructions of the Tully–Fisher relation in V (NGC 3344, Circinus) or in I (NGC 672, Maffei 2, Dwingeloo 1, and NGC 2903).

3.5.2 *Cepheids*

The adopted PL relations for Cepheids were

$$M_{V,\mathrm{Ceph}} = (-4.222 \pm 0.021) - (2.779 \pm 0.031)(\log P - 1) \quad (3)$$

$$M_{I,\mathrm{Ceph}} = (-4.923 \pm 0.014) - (2.979 \pm 0.021)(\log P - 1) \quad (4)$$

where $M_{V,\mathrm{Ceph}}$ and $M_{I,\mathrm{Ceph}}$ are the absolute magnitudes of the Cepheids in V and I, respectively, and P is the period of variability in days. Zero-points have been adjusted to the maser scale on the basis of the outcome of the pair-wise distance analysis described in Section 3.5.1. Zero-point errors do not include the uncertainty in the maser distance to M106, which is systematic.

For each galaxy with Cepheid observations, apparent distance moduli in V and I were combined to solve for the extinction and the extinction-free distance modulus simultaneously. Extinction coefficients and K-corrections were derived using the SED of a G0 supergiant. The extinction-free distance modulus, μ, was presumed to depend upon metallicity as follows (Freedman et al. 2001):

$$\mu = \mu_{\mathrm{true}} - \gamma(8.5 - \zeta). \quad (5)$$

Here μ_{true} is the true distance modulus, ζ is the mean logarithmic oxygen abundance by number [i.e. $12 + \log n(\mathrm{O})/n(\mathrm{H})$] at the location of the Cepheids as judged from H II regions (in a uniform way), and γ is a constant. The comparison of Cepheid distances with those from the TRGB yielded $\gamma = -0.180 \pm 0.047$.

3.5.3 *Planetary nebulae*

The luminosity in [O III]λ5007 of the brightest planetary nebulae (PNe) is a constant until the metallicity drops below a threshold (Ciardullo et al. 2002). In the past, corrections for metallicity below the threshold have been founded upon the mean oxygen abundance adopted for Cepheids, which has been based upon observations of H II regions. Typically, observed planetary nebulae are distributed differently from Cepheids, and of course come from an older population, so the mean metallicity of Cepheids is not necessarily representative. To determine distances from PNe, it is more sensible to use an index of the mass of the host galaxy as a proxy for metallicity. The index adopted here was the pseudo-absolute magnitude in K_s, M'_{Ks}, which would be computed from the unextinguished apparent magnitude of the galaxy, m_{Ks}, using a pseudo-distance modulus, μ', derived from a PNe luminosity limit equal to what would be observed in a high-metallicity system, where it appears to be a constant. Defining m^* to be the unextinguished apparent magnitude of the brightest PNe in [O III]λ5007, and M^{ref}_{Ks} to be the galaxian absolute magnitude threshold where the limit becomes sensitive to metallicity, then the absolute magnitude M^* of the PNe brightness limit was adopted to be

$$\begin{aligned} M^* &= z_P && \text{for } M'_{Ks} \le M^{\mathrm{ref}}_{Ks} \\ &= z_P + k_P \left[M'_{Ks} - M^{\mathrm{ref}}_{Ks}\right] && \text{for } M'_{Ks} > M^{\mathrm{ref}}_{Ks} \end{aligned} \quad (6)$$

where $M'_{Ks} = m_{Ks} - \mu'$, $\mu' = m^* - z_P$, and z_P and k_P are constants. The pairwise analysis of distances described in Section 3.5.1 yielded $M^{\mathrm{ref}}_{Ks} = -23.0 \pm 0.5$, $k_P = 0.106 \pm 0.049$, and $z_P = -4.573 \pm 0.042$ on the maser scale, where uncertainties are due to random errors only.

3.5.4 *Surface brightness fluctuations*

Absolute magnitudes in I of surface brightness fluctuations, $\overline{M}_I$, were derived from

$$\overline{M}_I = z_S + k_S \left[(V - I)_{\mathrm{bkg}} - 1.15)\right], \quad (7)$$

where $(V - I)_{\mathrm{bkg}}$ is the colour of the galaxy background where fluctuations are measured (Tonry et al. 2001), and z_S and k_S are constants. In correcting apparent fluctuation magnitudes for extinction, SEDs were approximated to be similar to that of an M4 giant. However, the SED of an elliptical galaxy was employed to correct the galaxy background colours. The value of k_S was adopted to be 4.5 ± 0.25 (Tonry et al. 2001), from which the pairwise distance analysis yielded $z_S = -1.700 \pm 0.066$ on the maser scale.

3.5.5 *Tip of the red giant branch*

Absolute magnitudes in I at the TRGB, $M_{I,\,TRGB}$, were derived from

$$M_{I,\mathrm{TRGB}} = z_T + k_T \left[(V - I)_{\mathrm{TRGB}} - 1.6\right], \quad (8)$$

where $(V - I)_{\mathrm{TRGB}}$ is the colour of the TRGB (Rizzi et al. 2007), and z_T and k_T are constants. In correcting apparent magnitudes for extinction, SEDs were approximated to be similar to that of an M0 giant. The value of k_T was adopted to be 0.217 ± 0.020 (Rizzi et al. 2007), from which the pairwise distance analysis yielded $z_T = -4.053 \pm 0.028$ on the maser scale.

3.5.6 *Fundamental Plane*

The I-band Fundamental Plane for dynamically hot systems was defined using galaxies in the Coma cluster (Fingerhut et al. 2003). The distance to the cluster was anchored to the I-band fundamental planes defined by the Leo I Group and the Fornax and Virgo clusters and to the I-band Tully–Fisher relation for *HST* Key Project galaxies with Cepheid distances (Freedman et al. 2001). Fundamental-Plane and Tully–Fisher distances to the Coma cluster from the Key Project were updated differentially by determining the mean shift in calibrator distances brought about by changes to the extinction, the introduction of K-corrections, and revisions to the PL relations for Cepheids, and also taking into account revisions to extinction and K-corrections for Coma galaxies. Revised distance moduli from the two methods differed by only 0.003 mag. The average was 34.753 ± 0.089 on the maser scale, which was adopted to set the zero-point of the Fundamental Plane. On the maser scale, the metric length R_e in kiloparsecs of the semimajor axis of the elliptical isophote encompassing half of the total light in I of a dynamically hot system was finalized to be

$$\begin{aligned} \log R_e = {} & (-7.74 \pm 0.69) + (0.83 \pm 0.06)\langle\mu\rangle_e/2.5 \\ & + (0.87 \pm 0.19) \log \sigma_{e8}, \end{aligned} \quad (9)$$

where $\langle\mu\rangle_e$ is the fully corrected mean 'face-on' surface brightness within the effective isophote in units of mag arcsec^{-2}, and σ_{e8} is the aperture-corrected velocity dispersion in units of km s^{-1}. For the Coma cluster calibrators, the rms scatter in $\log R_e$ was 0.09 dex (Fingerhut et al. 2003).

3.5.7 *Tully–Fisher relations*

In constructing Tully–Fisher relations, the amplitude of ordered motions was characterized by the tilt-corrected rotational velocity in the plateau of the rotation curve (V_{flat}), which is a more reliable

gauge of luminosity than the correspondingly corrected 21 cm line width (Verheijen 2001). For galaxies whose velocity fields were modelled with tilted rings, the tilt was adopted to be that displayed at radii in the plateau of the rotation curve. Relations in V and I were constructed using disc galaxies for which distances were derived from stellar indicators as described above. Calibrating galaxies were required to have $\log 2V_{\rm flat} \geq 2.1$, to be tilted by more than 40°, and to be extinguished by tilt by less than 0.75 mag in I. The V-band relation was established using the same set of galaxies as used for the I-band relation in order to reduce the chance of any systematic error in V-band distances with respect to I-band distances. From 29 galaxies, the following relations on the maser scale were derived :

$$M_{V,\rm TF} = (-20.793 \pm 0.044) - (8.539 \pm 0.284)\left[\log(2V_{\rm flat}) - 2.5\right] \quad (10)$$

$$M_{I,\rm TF} = (-21.656 \pm 0.050) - (9.243 \pm 0.315)\left[\log(2V_{\rm flat}) - 2.5\right]. \quad (11)$$

The rms scatter of the fits was 0.36 and 0.34 mag in V and I, respectively.

To judge the infrared luminosity of the Milky Way, galaxies in the Ursa Major cluster were employed to define the Tully–Fisher relation in K_s. This sample was selected because of the availability of good near-infrared photometry deeper than that of 2MASS carried out with arrays large compared to the galaxies (Tully et al. 1996; Verheijen & Sancisi 2001). Local galaxies were not employed due to the greater uncertainty in apparent magnitudes. To set the zero-point, the Key Project Tully–Fisher distance to the Ursa Major cluster (Freedman et al. 2001) was updated in the same way as that for the Coma cluster. This led to a distance modulus of 31.570 ± 0.121 on the maser scale. Selecting galaxies in the same way as for the Tully–Fisher relations in V and I, the following relation on the maser scale was derived from 18 cluster members:

$$M_{Ks,\rm TF} = (-23.483 \pm 0.077) - (11.384 \pm 0.563)\left[\log(2V_{\rm flat}) - 2.5\right]. \quad (12)$$

The rms scatter was 0.29 mag.

3.6 Luminosities

Luminosities were computed for sample galaxies from the adopted distances and adjusted fully-corrected K_s magnitudes. The luminosity of the Milky Way was estimated from the Tully–Fisher relation in K_s by adopting $V_{\rm flat}$ to be 226 ± 11 km s^{-1}. This value was based upon the recent upward revision of the rotation rate at the solar radius (Reid et al. 2009; van der Marel et al. 2012) and a comparison of observed and predicted shapes of rotation curves for the Milky Way (Xue et al. 2008; Sofue, Honma & Omodaka 2009; McMillan 2011), its look-alike NGC 891 (Sancisi & Allen 1979; Sofue 1997), and Andromeda (Carignan et al. 2006).

Fig. 2 displays the distribution of absolute magnitudes in K_s for sample galaxies. As seen elsewhere (Karachentsev & Kutkin 2005), there is a Gaussian-like peak centred around −24.0, with numbers declining for 1.5 mag faintward and then rising again until sampling becomes incomplete. The behaviour suggests that there are two superimposed populations, one luminous and one faint (Binggeli, Sandage & Tammann 1988). In this paper, the focus will be on the peak, namely galaxies with $M_{Ks} \leq -22.5$. These galaxies will be referred to as 'giants'.

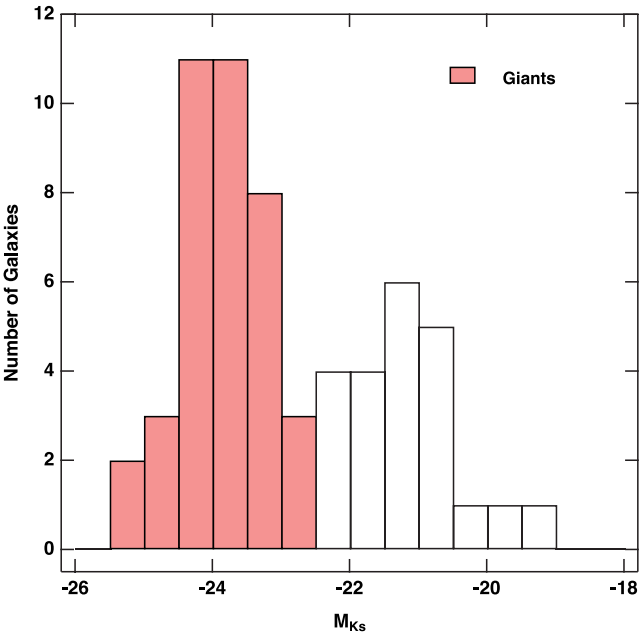

Figure 2. Luminosities of sample galaxies. The index of luminosity is the absolute magnitude in K_s. Galaxies designated as 'giants' are highlighted in pink.

4 ANALYSIS

4.1 The Local Sheet and Council of Giants

Past discussions of local structure have been guided by a coordinate system which is defined by the Local Supercluster. However, a fit of a plane to the positions of the eight giants and three interacting pairs of giants (luminosity-weighted) within 6 Mpc of the Milky Way reveals an extremely flattened aggregate inclined to the supergalactic plane by 7.°95 ± 0.°12 with a north pole at supergalactic coordinates (L, B) = (241.°74 ± 0.°74, 82.°05 ± 0.°12). Errors here stem from the uncertainties in distances alone. The Sun is perpendicularly offset northward of the mid-plane of the aggregate by 129 ± 4 kpc. Considering all giants individually, the standard deviation σ_z about the mid-plane is only 233 kpc. The apparent dispersion about the supergalactic plane is 357 kpc, which is 53 per cent higher. The dispersions are negligibly amplified by distance errors.

The plane just defined will be regarded in this paper as the mid-plane of the structure to be called the 'Local Sheet'. Discussions of the local organization of galaxies will be founded upon a coordinate system whose x–y plane is coincident with the mid-plane and whose x-axis points along the intersection with the supergalactic plane. This system will be referred to as 'Sheet coordinates'. Of the sample galaxies within 0.5 Mpc of the x–y plane, 87 per cent are less than 6 Mpc distant. Of the sample galaxies nearer than 6 Mpc, 81 per cent lie within 0.5 Mpc of the x–y plane.

Top and side views of the Local Sheet are presented in Fig. 3. To expose salient features, displays are presented in 'rotated Sheet coordinates', i.e. from the perspective generated by rotating the x-axis of Sheet coordinates by 107° clockwise around the z-axis. By restricting attention to luminous galaxies, and by limiting the region displayed to that part of the Local Volume where giants are most tightly confined, the figure shows more clearly than ever before the stark contrast between the Local Sheet and its surroundings.

Beyond Andromeda, all sample giants (and most non-giants) within 6 Mpc of the Sun are confined to a narrow annulus

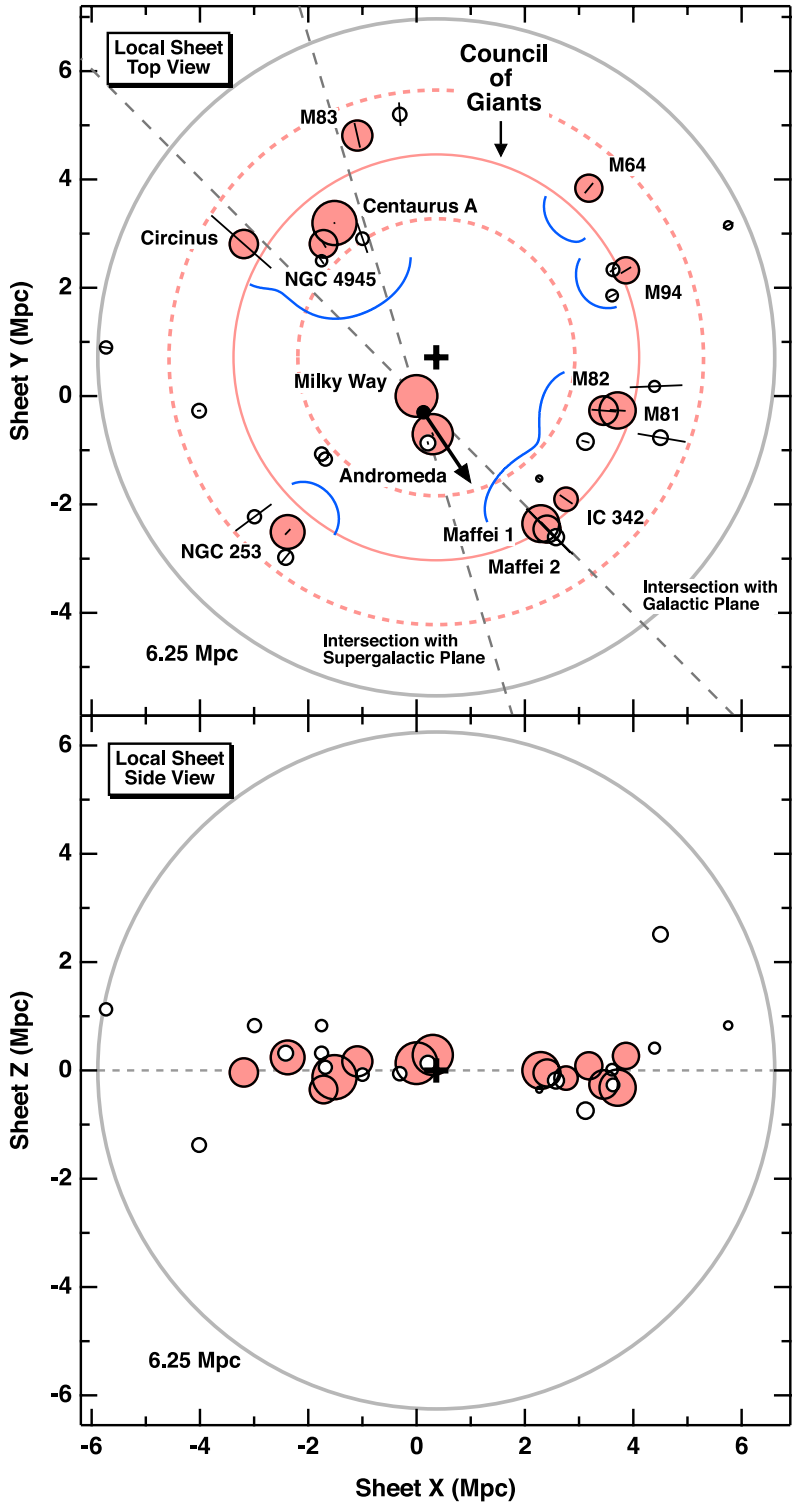

Figure 3. The spatial distribution of sample galaxies within 6.25 Mpc of the centre of the Council of Giants. Shown are top and side views in a coordinate system with an x–y plane coincident with the mid-plane of the Local Sheet, which is displayed as a dashed grey line in the lower panel. To optimize clarity, the x-axis of Sheet coordinates has been rotated 107° clockwise around the z-axis from the direction of the line of intersection with the supergalactic plane. In both panels, all sample galaxies within the spherical volume delineated by the large grey circles are displayed. Galaxies are marked by circlets whose diameters are proportional to the cube root of the stellar mass. Giants are highlighted in pink, and a bold cross marks the centre of the Council of Giants. In the top view, black bars superimposed upon the galaxy markers convey the uncertainties in distance. The luminosity-weighted centroid of the Local Group is noted with a small black disc, and the trajectory of the Local Group with respect to Council giants is conveyed by the attached arrow. The solid pink circle is the fit to the Council of Giants. The inner dashed pink circle marks the edge of the cylindrical realm of influence of the Local Group defined by density matching. The outer dashed pink circle correspondingly marks the outer edge of the density-matched volume of the Council. Curves in blue are the loci of potential maxima as viewed today from the centroid of the Local Group in directions parallel to the plane of the Sheet. Dashed grey lines mark the intersections of the Sheet with the Galactic and supergalactic planes.

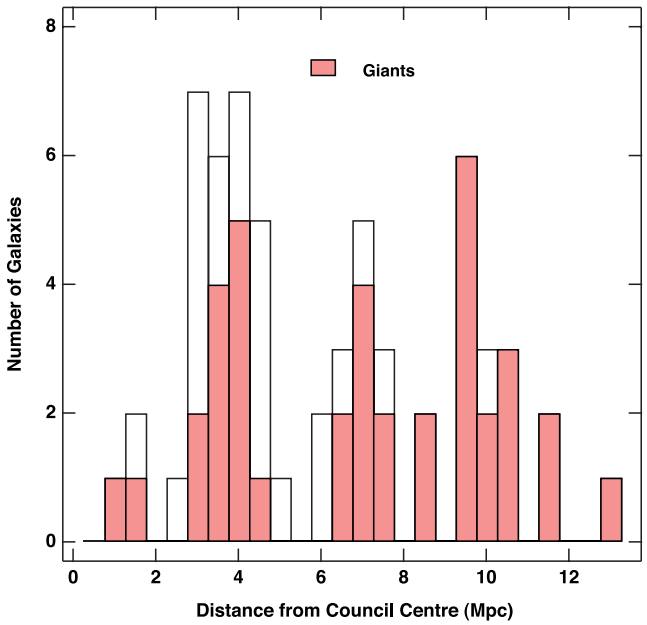

Figure 4. Distances of sample galaxies from the centre of the Council of Giants. Giants are highlighted in pink. The Council is evidenced by the peak centred at 3.75 Mpc.

encompassing the Local Group. This configuration will be referred to as the 'Council of Giants'. The Council clearly stands out in Fig. 4, which shows how sample galaxies are distributed over distance from its centre (defined below). Although it is by no means certain that the Council is anything more than an accidental arrangement of galaxies, it is worthy of its name by virtue of definitively limiting the extent of the Local Group's influence. Also, as will be shown below, angular momenta of members expose a degree of dynamical unity.

What is displayed in Fig. 3 are *all* galaxies within 6.25 Mpc of the *Council centre*. The circle best fitting the Council (handling binaries as before) has a radius of 3.746 ± 0.098 Mpc, where the uncertainty is from a Monte Carlo simulation accounting for random errors in distances only (the systematic error owing to the uncertainty in the distance zero-point is 0.113 Mpc). The fit is marked by a solid pink circle in Fig. 3. The cosmic standard deviation of radial positions is estimated to be 0.48 Mpc after distance uncertainties are removed. The centre of the Council (black cross) is 0.81 ± 0.13 Mpc from the Sun and offset along the Sheet from the centroid of the Local Group (small solid disc) by 1.06 Mpc. The only giant elliptical galaxies, Centaurus A and Maffei 1, sit on opposite sides of the Council, being separated in azimuth by 175°. Sample galaxies are tightly confined to the Local Sheet out to 4 Mpc from the centre, beyond which they start to become more widely dispersed vertically.

The 3σ edge of the giant component of the Local Sheet is 5.2 Mpc from the centre of the Council, at which position the histogram of distances displays a clear gap (Fig. 4). From this perspective, the 1σ thickness of the Sheet is only 5 per cent of the extent. Based upon a recent friends-of-friends analysis, dwarf irregular members of the Local Sheet are spread over an elliptical area whose boundary ranges 4.8 to 7.0 Mpc from the Council centre (Fingerhut 2012).

Relative to Council galaxies and pairs, the velocity of the Local Group along the plane of the Sheet is 11 ± 12 km s^{-1} away from the Council centre towards $-56° \pm 70°$ with respect to the displayed x direction of rotated Sheet coordinates. The vector is displayed as a thick black arrow in the top panel of Fig. 3. As viewed from the Council centre, the apex of the motion is 47° from the direction of the Local Group. The Council appears to be in radial equilibrium with respect to the Local Group, because after correction for the Group's translation, the mean of radially projected velocities is only -1 km s^{-1}, with a standard deviation of 51 km s^{-1}. Uncertainties in heliocentric velocities and distances account for 20 km s^{-1} of the spread, so the true velocity dispersion radial to the Council centre is 47 km s^{-1}. None of the results above change significantly if the Hubble constant is varied within the range of its uncertainty. As seen from the Sun, the velocity dispersion of isolated dwarf irregular galaxies with respect to the Local Group is 35 km s^{-1} (Fingerhut 2012), so motions of Council giants may be enhanced somewhat by the gravitational influence of neighbours.

Motions perpendicular to the Sheet are nearly tangential to the line of sight, so they cannot be measured reliably. However, cosmological simulations indicate that they may be just as cold as the radial motions (Fingerhut 2012). If so, then the time for a typical giant to pass through the Sheet (i.e. $2\sigma_z$, or 465 kpc) would be 9.6 Gyr, which is a significant fraction of the age of the Universe. The crossing time for isolated dwarfs is even longer (Fingerhut 2012). Thus, it appears that the galaxies in the Local Sheet have not had enough time to adjust dynamically to the gravitational environment in which they find themselves.

It is possible to determine unambiguously the direction of the spin angular momentum vector for most of the giants in the sample. Fig. 5 presents a Hammer projection displaying the directions of the vectors for giants within the Sheet (pink symbols) and beyond (black symbols) in rotated Sheet coordinates.

Spin angular momenta for Council giants (solid pink circlets) are aligned around a small circle with a radius of $71° \pm 14°$ and a pole which is $38° \pm 20°$ above the plane of the Sheet [at supergalactic coordinates $(L, B) = (125°, +41°)$]. Rotational angular momenta for the Milky Way and Andromeda (open pink circlets) point to the other side of the sky, the unweighted mean being 34° away from the antipode. The orbital angular momentum of Andromeda (pink diamond), estimated from the most recent measurement of the proper motion of Andromeda (van der Marel et al. 2012) using the revision to the heliocentric distance presented here, is on the side of the antipode, too, deviating 14° from the plane of the Sheet. However, because the orbit is nearly radial, this direction is extremely uncertain. Angular momentum vectors for giants beyond the Council (open black circlets) largely follow a great circle tilted by only $17° \pm 13°$ with respect to the Sheet plane and $23° \pm 13°$ with respect to the supergalactic plane. The three galaxies which deviate have angular momentum vectors pointing close to the poles. Notably, the unweighted mean spin vector for the Milky Way and Andromeda (open pink diamond labelled 'LG spin') points only 13° from the great circle.

The great circle's north pole, located at $(L, B) = (280°, +67°)$, is far from the small circle's pole, lying $70° \pm 24°$ away. Cumulative histograms of the deviations of angular momenta from the pole of the small circle further illustrate the differences between the two distributions (Fig. 6). A Kuiper test reveals that the probability that the two samples are drawn from the same population is only 2.3 per cent. In fact, this estimate should actually be regarded as an upper limit because the true nature of the distribution of spin orientations for giants not in the Council is smeared out in the cumulative histogram.

What is most important here (and missed previously by Kapranidis & Sullivan 1983) is that the angular momentum vectors of Council giants are ordered in a way which is completely different

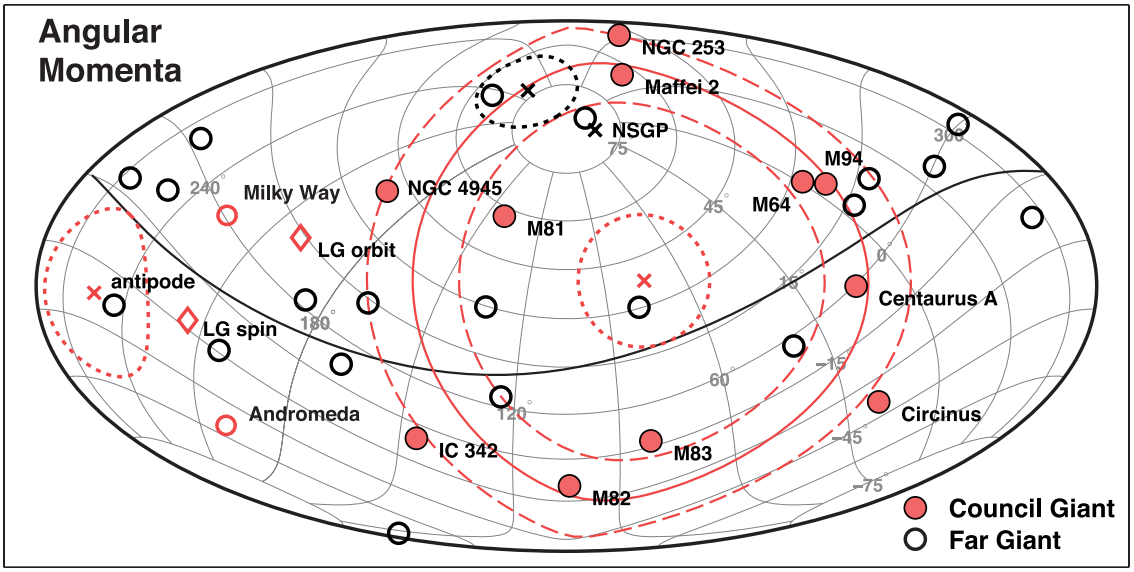

Figure 5. Angular momenta of galaxies in the Local Volume. Longitudes and latitudes of angular momentum vectors in rotated Sheet coordinates are conveyed via a Hammer projection. The coordinate system is the same as that of Fig. 3. For reference, the north pole of the supergalactic coordinate system is marked by a black cross labelled 'NSGP'. Pink markers and curves highlight features of giant galaxies in the Local Sheet, whereas black is reserved for giant galaxies beyond. Solid pink circlets mark the directions of rotational angular momentum vectors for Council giants. Open pink circlets show them for the Milky Way and Andromeda, and the open pink diamond labelled 'LG spin' (215°, −28°) marks the unweighted mean. The open pink diamond labelled 'LG orbit' (200°, +14°) depicts the orbital angular momentum of Andromeda. The solid pink curve is the small circle best fitting the locus of spin vectors of giants in the Council. Concentric dashed pink circles outline the extent of the uncertainty in the cone angle. The pole of the small circle (74°, +38°) and its uncertainty are marked by a pink cross and enclosing small dotted pink circle, respectively. The opposite pole and error circle are marked with a pink cross labelled 'antipode' and a surrounding dotted pink circle, respectively. Open black circlets depict the directions of rotational angular momentum vectors for giants beyond the Local Sheet, and the heavy black curve is the great circle fitting all but the three close to the Sheet poles. The north pole of the great circle (250°, +73°) and its corresponding error circle are marked by a black cross and enclosing dotted black circle, respectively. For most galaxies, the uncertainty in the direction of the spin vector is smaller than the symbol depicting it.

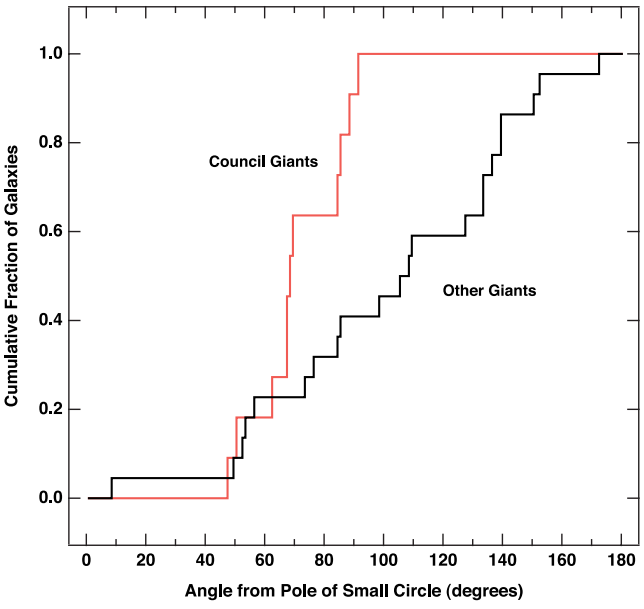

Figure 6. Cumulative histograms of spin directions relative to the small circle pole defined by the angular momenta of Council giants. The histogram for Council giants is shown in pink. The histogram for giants beyond the Council or in the Local Group is shown in black.

from what is seen for giants beyond. In this sense, the Local Sheet is dynamically distinct from the Local Supercluster. Angular momentum vectors for dark matter haloes in a sheet are predicted to align with the plane of the sheet (Bailin & Steinmetz 2005; Libeskind et al. 2012), so the observed spins of giants beyond the Council, and perhaps even the Milky Way and Andromeda, may reflect order associated with flattening on larger scales, such as that of the Local Supercluster. There is a hint that even the Council giants once followed this pattern; the pole of the small circle reflects the mean direction of their angular momenta, and it is located only $20° \pm 24°$ from the great circle along which vectors for more distant giants are arranged. It is unknown how the present arrangement of Council vectors developed, but one might speculate that it is somehow tied to torquing arising from the embedded asymmetry embodied by the mass distribution of the Local Group (Longair 2008).

4.2 Range and overdensity of the Local Group

The Council of Giants defines a clear upper bound to the extent of matter which contributed to the formation of the Local Group. In fact, its size can be used to judge the 'realm of influence' of the Group and, in turn, the overdensity of the Local Sheet. Suppose that the matter in the Local Group is spread above and below the Sheet in a cylinder around the Council centre having radius $R_{\rm LG}$. Suppose also that the matter of the Council is dispersed contiguously in a cylindrical shell with the same vertical dimension and extending inwards to $R_{\rm LG}$ from its observed radius R_C and outwards by an equal amount to $R_{\rm edge}$. One might expect $R_{\rm edge} - R_C$ to equal $R_C - R_{\rm LG}$ if the driver of evolution is gravity. From the standpoint of continuity, there must be a value of $R_{\rm LG}$ within which the density of matter associated with the Local Group matches the density of matter associated with Council galaxies. This radius defines the extent of the volume which could have contributed to the development of the Local Group, as well as the extent of the zone over which the

Council prevailed. The ratio $R_{\rm LG}/R_C$ is determined solely by the ratio of the mass contained in Council galaxies, $\mathcal{M}_C$, to the mass contained in the Local Group, $\mathcal{M}_{\rm LG}$:

$$R_{\rm LG}/R_C = 2\left[(\mathcal{M}_C/\mathcal{M}_{\rm LG}+1)^{1/2}+1\right]^{-1}. \quad (13)$$

It is reasonable to presume that non-giants constitute comparable and relatively small fractions of the mass in the Local Group and the Council (Karachentsev et al. 2004), so giants alone can be used to judge $\mathcal{M}_C/\mathcal{M}_{\rm LG}$ reliably. However, to do so, the ratio of dark to baryonic mass in the Council relative to the Local Group must be constrained.

The most recent study of weak lensing (Velander et al. 2014) has quantified masses for galaxies within the virial radius, i.e. within the radius at which the density of matter exceeds the cosmic average by a factor of 200. The ratio of this 'virial mass' to the stellar mass for galaxies with spiral-like colour classes is constant within errors for stellar masses spanning the range $0.2\text{–}4\times10^{10}\,h_{70}^{-2}\,\mathcal{M}_\odot$, i.e. over most of the range covered by giant spirals in the Local Sheet ($h_{70}=H_0/70\,{\rm km\,s^{-1}\,Mpc^{-1}}$ is a scaled value of the Hubble constant). Thus, a fixed stellar mass fraction for spirals is reasonable. There is evidence that the virial-to-stellar mass ratio for galaxies with elliptical-like colour classes does vary slowly with stellar mass over the range $2\text{–}40\times10^{10}\,h_{70}^{-2}\,\mathcal{M}_\odot$, but in the mass range of interest here such galaxies appear to have stellar mass fractions comparable to those of spirals. Taken at face value, the results indicate that the ratio of the virial to the stellar mass for Maffei 1 and Cen A should exceed that of the Milky Way by factors of 1.3 and 1.5, respectively. Nevertheless, Velander et al. (2014) caution that such a comparison is precarious because different mass ranges are probed by the two colour classes. As a baseline for this paper, the total mass of every giant has been assumed to be a fixed multiple of its stellar mass. This approximation does not lead to a large error in $\mathcal{M}_C/\mathcal{M}_{\rm LG}$ or in quantities derived from it because the two elliptical galaxies in the Council constitute only 36 per cent of the stellar mass there (see Table 4). Note that stellar masses are likely to be better indices of total masses than baryonic masses (i.e. stars plus gas). Baryonic masses under-weight ellipticals relative to spirals because gas expelled by ellipticals is missed.

Stellar masses were determined from luminosities in K_s utilizing mass-to-light ratios estimated from chemo-photometric models by Portinari, Sommer-Larsen & Tantalo (2004) founded upon the initial mass function (IMF) of Kroupa (1998). Syntheses by Portinari et al. (2004) were chosen because of the careful attention given to asymptotic giants and the realistic construction of composite systems of stars. The Kroupa IMF is superior to that of Salpeter (Salpeter 1955) because it yields synthetic mass-to-light ratios in B, V, I, and K which agree well with the values observed locally for the disc of the Milky Way (Portinari et al. 2009). Specifically, stellar mass-to-light ratios were estimated from integrated $B-V$ colours using

$$\log \mathcal{M}_{\rm stars}/\mathcal{L}_{Ks} = -0.298 + 0.73\left[(B-V)-0.6\right]. \quad (14)$$

In converting absolute magnitudes to luminosities, the absolute magnitude of the Sun in K_s was adopted to be 3.315 (Flynn et al. 2006; Holmberg, Flynn & Portinari 2006). Fortunately, mass-to-light ratios in K_s do not vary steeply with colour, so despite their uncertainty, relative stellar masses can be computed with some confidence.

Stellar masses for the giant galaxies yield $\mathcal{M}_C/\mathcal{M}_{\rm LG}=2.72\pm0.54$. Then, density matching leads to $R_{\rm LG}=2.56\pm0.17$ Mpc. Correspondingly, the outer boundary of the shell in which the smoothed density of Council giants matches that of the Local Group is at radius $R_{\rm edge}=4.94\pm0.27$ Mpc. Note that errors here do not include the uncertainty in the distance zero-point. In Fig. 3, $R_{\rm LG}$ and $R_{\rm edge}$ are marked by dashed pink circles.

Table 4 shows how $\mathcal{M}_C/\mathcal{M}_{\rm LG}$, $R_{\rm LG}$, and $R_{\rm edge}$ depend upon input assumptions. Changes are within errors if the stellar mass-to-light ratios are held fixed or if total-to-stellar mass ratios follow the trends suggested by weak lensing. The value of $R_{\rm LG}$ increases by 15 per cent if a spherical geometry is adopted. If the specification of $R_{\rm edge}$ is modified to require that the mass of the Council be distributed equally between a shell with width $R_{\rm edge}-R_C$ and a shell with width $R_C-R_{\rm LG}$, i.e. to require the Council to have accumulated just as much mass from beyond R_C as from within, then $R_{\rm LG}$ decreases slightly because the density overall must rise in response to the reduced volume of the outer shell. Again, the change is within the uncertainty.

It is possible to estimate the overdensity, Δ, of the Local Sheet, defined here as the ratio of the observed matter density to the mean for the Universe, by comparing the mass of the Local Group with the mass of matter expected within its realm of influence at the background density. To this end, the cylindrical

Table 4. Sensitivities of derived parameters to input.

Input	$\mathcal{M}_C/\mathcal{M}_{\rm LG}$ (1)	$R_{\rm LG}$ (2)	$R_{\rm edge}$ (3)	Δ (4)	Efficiency $\times\,\Delta$ (5)
Baseline [a]	2.72 ± 0.54	2.56 ± 0.17	4.94 ± 0.27	1.04 ± 0.25	0.365 ± 0.060
$\mathcal{M}_{\rm stars}/\mathcal{L}_{Ks}$ fixed [b]	2.26 ± 0.45	2.67 ± 0.18	4.82 ± 0.26	0.92 ± 0.21	0.322 ± 0.054
$\mathcal{M}_{\rm total}/\mathcal{M}_{\rm stars}$ variable [c]	3.19 ± 0.65	2.46 ± 0.17	5.03 ± 0.27	1.17 ± 0.29	0.410 ± 0.069
Spherical Geometry	2.72 ± 0.54	2.94 ± 0.17	4.55 ± 0.24	1.03 ± 0.22	0.361 ± 0.065
Equal-mass Shells [d]	2.72 ± 0.54	2.44 ± 0.18	4.70 ± 0.24	1.21 ± 0.31	0.421 ± 0.070

(1) Mass of Council relative to mass of Local Group; (2) radius of boundary of Local Group, in Mpc; (3) radius of outer boundary of Council, in Mpc; (4) factor by which mass of Local Group judged from timing exceeds that derived by density matching. (5) fraction of mass of galaxies which is stellar relative to cosmic fraction of matter which is baryonic as judged from density matching alone (without correcting for the overdensity).

[a] $\mathcal{M}_{\rm stars}/\mathcal{L}_{Ks}$ derived from $B-V$ using algorithm of Portinari et al. (2004); $\mathcal{M}_{\rm total}/\mathcal{M}_{\rm stars}$ fixed; Cylindrical geometry; Council boundaries equidistant from Council.

[b] $\mathcal{M}_{\rm stars}/\mathcal{L}_{Ks}$ set to baseline value for $B-V=0.6$.

[c] Relative values of total mass constrained by trends in $\mathcal{M}_{\rm total}/\mathcal{M}_{\rm stars}$ with $\mathcal{M}_{\rm stars}$ as revealed by weak lensing (Velander et al. 2014).

[d] Council boundaries defined by mass-matching.

volume through which matter is dispersed is approximated to have height equal to $2R_{\rm LG}$. The matter density parameter derived by the Planck consortium [Ade et al. (Planck Collaboration) 2013] is $\Omega_{\rm m}\,h^2 = 0.1426 \pm 0.0025$ ('Planck + WP'), where $h = H_0/100\,{\rm km\,s^{-1}\,Mpc^{-1}}$. Thus, within the cylinder, $\mathcal{M}_{\rm LG}/\Delta = (4.16 \pm 0.85) \times 10^{12}\,\mathcal{M}_\odot$, independent of h. This is close to the mass of the Local Group as judged from timing (van der Marel et al. 2012), which is $(4.34 \pm 0.54) \times 10^{12}\,\mathcal{M}_\odot$ after accounting for revisions to the heliocentric distance and total heliocentric velocity of Andromeda (this work) and to the age of the Universe [Ade et al. (Planck Collaboration) 2013]. The corresponding overdensity is 1.04 ± 0.25. The overdensity rises to 1.21 ± 0.47 if cosmological simulations are employed to virialize the timing mass (van der Marel et al. 2012).

The estimate for the overdensity does not depend strongly on input parameters (see Table 4). Notably, it is insensitive to the choice of geometry. Of course, it would be higher if there were significant amounts of matter beyond the Local Group not incorporated in galaxies (see Fingerhut 2012). However, the result fits expectations from models of the velocity field of galaxies within $40\,h^{-1}$ Mpc (Klypin et al. 2003), which predict an overdensity of about unity within $5\,h^{-1}$ Mpc.

Most of the light of the Local Group comes from its two giants, so the total mass-to-light ratio in K_s gleaned from density matching is $(8.9 \pm 1.5)\Delta$ in solar units. For Sheet giants overall, it is somewhat greater, $(10.1 \pm 1.7)\Delta$, because of the enhanced stellar mass-to-light ratios of the ellipticals. The timing mass for the Local Group implies a total-to-stellar mass ratio for spiral galaxies of 18.5 ± 4.1, which is significantly lower than the value of 43 ± 9 suggested by weak lensing.

Comparing the fraction of the mass of Sheet giants in stellar form with the cosmic ratio of baryons to matter, density matching yields an efficiency of galaxy formation (Ostriker & Naab 2012) equal to $(0.365 \pm 0.060)/\Delta$. Utilizing the timing mass for the Local Group, the efficiency works out to 0.349 ± 0.077. The estimates must be regarded as lower limits to the true efficiency because gas incorporated in galaxies has not been accommodated. How the estimate for the efficiency derived from density matching depends upon input parameters is summarized in Table 4.

If all matter within $r_{\rm edge}$ were dispersed evenly across the plane of the Sheet, the surface mass density would be $(0.202 \pm 0.014)\Delta\,\mathcal{M}_\odot\,{\rm pc^{-2}}$. This corresponds to 0.092 ± 0.027 Milky Ways per square Megaparsec, independent of Δ.

4.3 Evolution of the Local Group

The reservoir of matter available to contribute to the development of the Local Group must have been limited by the gravitation of surrounding material. In the upper panel of Fig. 3, blue curves trace maxima in the potential surface described by the gravitational fields of the 14 giants in the Local Sheet as viewed today from the luminosity-weighted centroid of the Local Group. Relative masses were gauged from stellar masses assuming a fixed total-to-stellar mass ratio. Council galaxies, especially the ellipticals, clearly restrict the domain of the Local Group. If mass equivalent to the Local Group giants is placed at the centre of the Council, and mass equivalent to Council giants is uniformly spread around the Council at radius R_C, then the potential in the plane of the Sheet peaks at a radius of 2.6 Mpc. This is identical to the radius of the realm of influence of the Local Group derived from density matching. Neither result depends on the mass scale, and sensitivities to relative masses are extremely weak.

Because of the unique arrangement of galaxies in the Council, the two elliptical galaxies would have gravitationally confined any mass concentration in the Council in two orthogonal directions. It is conceivable that galaxies in the Canes Venatici I group (NGC 4736 and NGC 4826) and the Sculptor group (NGC 253) were particularly vulnerable, given that the ellipticals are roughly equidistant.

There is additional, albeit circumstantial, evidence that the development of the Local Group was influenced by local structure. The position vector of Andromeda with respect to the Milky Way is inclined by only 11° with respect to the Local Sheet. Projected on to the Sheet, it deviates by only 11° from the axis of the ellipticals. Furthermore, accounting for tangential motion (van der Marel et al. 2012), the current trajectory of Andromeda is at an angle of only 3° with respect to the plane of the Sheet in a direction 13° from the elliptical axis. These observations hint that binarity may have been connected somehow to the existence of the elliptical dipole.

Studies of the spatial anisotropy of dwarfs in the Local Group also suggest a connection with the organization of matter beyond the Local Group (Pasetto & Chiosi 2007; Lee & Lee 2008). The axis of least dispersion is 29° from the pole of the Local Sheet, and the potential field inferred from the axis of greatest dispersion suggests that tidal forces are maximized in a direction only 8° to 15° away from Maffei 1. The recently discovered extended array of dwarf galaxies in orbit around the Andromeda galaxy (Ibata et al. 2013; Conn et al. 2013) occupies a plane inclined by only 18° to the Local Sheet. Such a close alignment would be expected if the system were an outcome of an interaction of bodies confined to moving within a pre-existing flattened framework of matter.

Along the line joining the two elliptical galaxies, the potential from Council galaxies (i.e. excluding the influence of the Milky Way and Andromeda) peaks 0.3 Mpc from the Council centre (0.8 Mpc from the centroid of the Local Group). There is a broad shallow minimum in the perpendicular direction. Thus, the centre represents a point of instability. If the Local Group started there, it would likely have moved in the general direction of an elliptical. Indeed, projected on to the Local Sheet, the Local Group is moving away from the Council centre in the direction of Maffei 1 on a trajectory which is only 1° from parallel to the axis of the ellipticals. However, at the current position of the Local Group, the potential arising from Council giants as they are configured today is 3 per cent higher than at the centre (a barrier of $30\,{\rm km\,s^{-1}}$). Also, even after augmenting the translational motion by 3σ, the Local Group would be able to move only 60 per cent of the way from the centre to its present position in a time less than the age of the Universe. Consequently, in a relative sense, it is likely that the Local Group developed at a place offset from the Council centre.

5 DISCUSSION

Being giant elliptical galaxies, it is likely that both Maffei 1 and Centaurus A developed strong winds during their evolution as a result of heating by massive stars and supernovae (Mathews & Baker 1971; Larson 1974; Matteucci & Pipino 2002; Pipino & Matteucci 2004; Pinsonneault, Martel & Pieri 2010; Côté et al. 2012). During the Sedov–Taylor phase of their expansion, the winds could have shepherded gas located between the two galaxies, possibly contributing to the growth of discs in the Local Group. The winds might also have had a bearing on confining gas and triggering star formation in nearby galaxies. Stellar velocity dispersions offer a means of probing the salient details (McCall, Richer & Stasińska 1998; McCall & Richer 2003).

An energy-driven wind would have developed once the gas temperature rose to the virial temperature, which is set by the potential. That temperature can be gauged today from the kinetic energy per unit mass of stars, u_s, assuming that dark matter dominates the mass. The velocity dispersions for Maffei 1 and Cen A are $180 \pm 7\,\mathrm{km\,s^{-1}}$ and $126 \pm 9\,\mathrm{km\,s^{-1}}$, respectively, after correction to a radius equal to one-eighth of the effective radius (Dufour et al. 1979; Fingerhut et al. 2003; Silge et al. 2005). Thus, the virial temperatures for Maffei 1 and Cen A are $(2.4 \pm 0.2) \times 10^6$ K and $(1.2 \pm 0.2) \times 10^6$ K, respectively. The escape velocity is supersonic at the virial temperature, and the terminal velocity of ejected gas could have been as high as three times the speed of sound, i.e. $(700 \pm 30)\,\mathrm{km\,s^{-1}}$ in the case of Maffei 1 and $(490 \pm 30)\,\mathrm{km\,s^{-1}}$ in the case of Cen A (Khare 1953; Pack 1953; Chevalier & Clegg 1985; Murray, Quataert & Thompson 2005; Oppenheimer & Davé 2006). At the time of the wind, the internal energy of gas heated by stellar processes would have been linked to the total mass of stars formed, $\mathcal{M}_s$. Consequently, the virial condition for mass loss requires that the mass of gas that was ejected be proportional to $\mathcal{M}_s/u_s$. Because the stellar mass of Cen A is 1.7 ± 0.7 times greater than that of Maffei 1, Cen A would have ejected 3.5 ± 1.6 times more gas, and the Sedov–Taylor radius would have been 1.5 ± 0.2 times larger (McKee & Truelove 1995). If the overdensity of intergalactic baryons were comparable to or below that estimated for all matter, then the ejected gas could have expanded freely all the way to the Local Group. For example, if gas left Maffei 1 at a redshift of 2.5 or Cen A at a redshift of 5.0, it would have reached the Local Group by a redshift of 1.5, the epoch of peak star formation 9.5 billion years ago (Soifer, Helou & Werner 2008). Thus, it is feasible that gas expelled from the Council ellipticals could have influenced the baryonic evolution of disc galaxies in the Local Sheet.

How well the Local Sheet retains intergalactic baryons, be they primordial or from galactic winds, depends upon its virial temperature. The virial temperature $T_{\rm vir}$ near the mid-plane of a sheet with radius R and surface mass density Σ is given by

$$T_{\rm vir} = \frac{2\pi G}{3k} A m_{\rm p} \Sigma R, \tag{15}$$

where G is the gravitational constant, k is Boltzmann's constant, A is the mean molecular weight, and $m_{\rm p}$ is the mass of the proton. Adopting a radius of 5.2 Mpc for the giant component, the estimated mean surface mass density of matter implies a virial temperature of 7×10^5 K and an escape velocity of $240\,\mathrm{km\,s^{-1}}$. Fingerhut (2012) has suggested that there may be as much as a factor of 2 more mass in the Sheet than is found in galaxies, so the actual virial temperature could easily be over a million degrees. Therefore, warm gas may permeate the Sheet, but gas ejected by the ellipticals in directions at large angles to the Sheet would have escaped.

6 CONCLUSIONS

Properties of the Local Sheet and its Council of Giants are summarized in Table 5. This study suggests that a structure with the geometry of the Sheet was instrumental in guiding the formation and evolution of constituent galaxies. It also suggests that a binary, or the precursor of it, can influence the angular momentum acquired

Table 5. The Local Sheet.†

Parameter	Units	Value	Parameter	Units	Value
1. Giant Membership		14	14. Stellar luminosity	$\mathcal{L}_{\odot,Ks}$	1.53×10^{12}
2. (L, B) of North Pole	deg	(241.74, +82.05)	15. Stellar mass	$\mathcal{M}_\odot$	8.7×10^{11}
3. Tilt	deg	7.95	16. Total mass	$\mathcal{M}_\odot$	1.6×10^{13}
4. Offset from Sun	Mpc	0.129	17. Total mass/Stellar mass		18.5
5. Thickness	Mpc	0.465	18. Local Group fraction		0.27
6. Extent	Mpc	10.4	19. Elliptical fraction		0.27
7. (X, Y, Z) of Council Centre	Mpc	(−0.25, +0.77, −0.05)	20. Surface Mass density	$\mathcal{M}_\odot\,\mathrm{pc^{-2}}$	0.21
8. Council Diameter	Mpc	7.49	21. Velocity dispersion	$\mathrm{km\,s^{-1}}$	47
9. Separation of Ellipticals	Mpc	6.73	22. Crossing time	Gyr	9.6
10. Angle between Ellipticals	deg	175.0	23. Virial temperature	K	7.3×10^5
11. (L, B) of Council Spin Pole	deg	(125.1, +41.5)	24. Escape velocity	$\mathrm{km\,s^{-1}}$	244
12. Local Group Realm	Mpc	5.11	25. Overdensity		1.04
13. Tilt of Local Group	deg	11.3	26. Efficiency		0.35

(1) Number of members with $M_{Ks} \leq -22.5$. (2) Supergalactic longitude and latitude of north pole of Local Sheet. (3) Inclination of plane of Local Sheet with respect to supergalactic plane. (4) Perpendicular offset of plane of Local Sheet from the Sun. (5) Twice the standard deviation of giants about the plane. (6) The diameter, as given both by the radius of the Council of Giants augmented by three times the standard deviation of the members and by the radius of the edge of the density-matched zone of the Council of Giants augmented by its uncertainty. (7) Supergalactic Cartesian coordinates of the centre of the Council of Giants. (8) Diameter of the Council of Giants. (9) Physical separation of Maffei 1 and Centaurus A. (10) Angular separation of Maffei 1 and Centaurus A projected on to the Sheet plane, as seen from the centre of the Council of Giants. (11) Supergalactic longitude and latitude of pole of angular momentum vectors for Council giants. (12) Diameter of the zone of influence of the Local Group, as indicated by both density matching and the potential surface of the Sheet. (13) Tilt of the Andromeda–Milky Way axis to the plane of the Sheet. (14) Total luminosity of giants in K_s. (15) Stellar mass of giants, based upon luminosities in K_s and mass-to-light ratios derived from $B - V$ colours using the algorithm of Portinari et al. (2004). (16) Total mass of giants, based upon the mass scale defined by the timing mass of the Local Group. (17) Ratio of total mass of giants to stellar mass of giants. (18) Fraction of the mass of the Sheet in the Local Group. (19) Fraction of the mass of the Sheet in giant ellipticals. (20) Smoothed mass of giants per unit area. (21) Radial dispersion of velocities of Council giants with respect to the Council centre. (22) Time to cross the thickness of the Sheet for a galaxy moving vertically with a velocity equal to the velocity dispersion radially. (23) Temperature expected for a virialized gas with an extent equal to that of the Sheet if the mass of galaxies were uniformly spread over that extent. (24) Vertical velocity required to escape the mid-plane based upon the surface mass density and extent of the Sheet. (25) Factor by which mass of the Local Group judged from timing exceeds that derived from density-matching. (26) Fraction of the mass of galaxies which is stellar relative to the cosmic fraction of matter which is baryonic.

†Properties are founded upon a distance scale set by M106 (NGC 4258), the distance to which was adopted to be the geometric maser estimate 7.60 Mpc (Humphreys et al. 2013). The distance to the centre of the Milky Way was adopted to be 8.29 kpc (van der Marel et al. 2012). Velocity corrections were based upon a Hubble constant of $71.6\,\mathrm{km\,s^{-1}\ Mpc^{-1}}$ (Riess et al. 2011, 2012; Humphreys et al. 2013). Uncertainties in tabulations are discussed in the text.

by neighbouring galaxies. It is unlikely that a randomly dispersed collection of galaxies could have agglomerated into a structure as cold as the Sheet in a way which could generate an interacting pair of galaxies near the middle of a ring of galaxies with opposing ellipticals and ordered spins. Indeed, modern cosmological simulations reveal galaxies developing from dark cores fed by flows of gas along pre-existing filaments of dark matter (Danovich et al. 2012).

Unfortunately, there is only one Local Sheet. Further insights into the formation and evolution of the Local Sheet, and particularly guidance on the interplay between the Local Group and the Local Sheet, will require the identification of like systems in the greater Universe.

ACKNOWLEDGEMENTS

The author thanks R. Fingerhut for many stimulating conversations about the Local Sheet as she progressed in her investigations of the dwarf component, and for her comments on the first draft of this paper. The author is grateful to S. Sakai for her help in understanding the foundations of the Key Project Tully–Fisher relations and to K. Herrmann for her assistance in interpreting her measurements of luminosity functions of planetary nebulae. Thanks are conveyed also to R. M. Stesky of Pangaea Scientific for support with Spheristat, a geophysical software package seconded to study the organization of angular momentum vectors, and to G. Conidis for statistical insights. Particular gratitude is expressed to S. McCall, A. Boudakian, M. Doherty, C. Law, J. Marshall, M. Ng, and F. Shariff, whose attention to the author's health allowed this work to be completed, and to N. McCall for thought-provoking discussions and for his strength during times of adversity. Finally, the author is grateful to the Natural Sciences and Engineering Research Council of Canada for its continuing support.

REFERENCES

Ables H. D., 1971, Publications of the U.S. Naval Observatory Second Series, 20
Achtermann J. M., Lacy J. H., 1995, ApJ, 439, 163
Ade P. A. R. et al. (Planck Collaboration), 2013, preprint (arXiv:1303.5076)
Adler D. S., Westpfahl D. J., 1996, AJ, 111, 735
Aguerri J. A. L., Debattista V. P., Corsini E. M., 2003, MNRAS, 338, 465
Annibali F., Aloisi A., Mack J., Tosi M., van der Marel R. P., Angeretti L., Leitherer C., Sirianni M., 2008, AJ, 135, 1900
Bailin J., Steinmetz M., 2005, ApJ, 627, 647
Bajaja E., van der Burg G., Faber S. M., Gallagher J. S., Knapp G. R., Shane W. W., 1984, A&A, 141, 309
Barbon R., Capaccioli M., 1975, A&A, 42, 103
Begeman K. G., 1987, PhD thesis, Kapteyn Institute
Bertola F., Cinzano P., Corsini E. M., Rix H.-W., Zeilinger W. W., 1995, ApJ, 448, L13
Binggeli B., Sandage A., Tammann G. A., 1988, ARA&A, 26, 509
Blakeslee J. P., Lucey J. R., Barris B. J., Hudson M. J., Tonry J. L., 2001, MNRAS, 327, 1004
Bottema R., Shostak G. S., van der Kruit P. C., 1986, A&A, 167, 34
Bridzius A., Vansevicius V., 2001, Balt. Astron., 10, 413
Burkhead M. S., 1986, AJ, 91, 777
Burton W. B., Verheijen M. A. W., Kraan-Korteweg R. C., Henning P. A., 1996, A&A, 309, 687
Busarello G., Capaccioli M., D'Onofrio M., Longo G., Richter G., Zaggia S., 1996, A&A, 314, 32
Buta R., 1988, ApJS, 66, 233
Buta R. J., McCall M. L., 1999, ApJS, 124, 33
Butler D. J., Martínez-Delgado D., Brandner W., 2004, AJ, 127, 1472
Caon N., Macchetto D., Pastoriza M., 2000, ApJS, 127, 39
Capaccioli M., Held E. V., Nieto J.-L., 1987, AJ, 94, 1519
Capaccioli M., Held E. V., Lorenz H., Vietri M., 1990, AJ, 99, 1813
Capaccioli M., Cappellaro E., Held E. V., Vietri M., 1993, A&A, 274, 69
Cappellari M. et al., 2007, MNRAS, 379, 418
Carignan C., 1985, ApJS, 58, 107
Carignan C., Puche D., 1990, AJ, 100, 641
Carignan C., Chemin L., Huchtmeier W. K., Lockman F. J., 2006, ApJ, 641, L109
Casertano S., van Gorkom J. H., 1991, AJ, 101, 1231
Chevalier R. A., Clegg A. W., 1985, Nature, 317, 44
Ciardullo R., Jacoby G. H., Ford H. C., Neill J. D., 1989a, ApJ, 339, 53
Ciardullo R., Jacoby G. H., Ford H. C., 1989b, ApJ, 344, 715
Ciardullo R., Jacoby G. H., Harris W. E., 1991, ApJ, 383, 487
Ciardullo R., Feldmeier J. J., Jacoby G. H., Kuzio de Naray R., Laychak M. B., Durrell P. R., 2002, ApJ, 577, 31
Ciardullo R., Durrell P. R., Laychak M. B., Herrmann K. A., Moody K., Jacoby G. H., Feldmeier J. J., 2004, ApJ, 614, 167
Conn A. R. et al., 2013, ApJ, 766, 120
Copin Y., Cretton N., Emsellem E., 2004, A&A, 415, 889
Côté B., Martel H., Drissen L., Robert C., 2012, MNRAS, 421, 847
Crosthwaite L. P., Turner J. L., Buchholz L., Ho P. T. P., Martin R. N., 2002, AJ, 123, 1892
Curran S. J., Koribalski B. S., Bains I., 2008, MNRAS, 389, 63
Dahlem M., Golla G., Whiteoak J. B., Wielebinski R., Huettemeister S., Henkel C., 1993, A&A, 270, 29
Dahlem M., Ehle M., Ryder S. D., Vlajić M., Haynes R. F., 2005, A&A, 432, 475
Daigle O., Carignan C., Amram P., Hernandez O., Chemin L., Balkowski C., Kennicutt R., 2006, MNRAS, 367, 469
Danovich M., Dekel A., Hahn O., Teyssier R., 2012, MNRAS, 422, 1732
de Blok W. J. G., Walter F., Brinks E., Trachternach C., Oh S.-H., Kennicutt R. C., Jr, 2008, AJ, 136, 2648
de Jong R. S., van der Kruit P. C., 1994, A&AS, 106, 451
de Vaucouleurs G., 1953, AJ, 58, 30
de Vaucouleurs G., 1958, ApJ, 128, 465
de Vaucouleurs G., 1959, ApJ, 130, 728
de Vaucouleurs G., 1964, ApJ, 139, 899
de Vaucouleurs G., 1975, ApJ, 202, 319
de Vaucouleurs G., Caulet A., 1982, ApJS, 49, 515
de Vaucouleurs G., Davoust E., 1980, ApJ, 239, 783
de Zeeuw P. T. et al., 2002, MNRAS, 329, 513
Dressler A., Sandage A., 1983, ApJ, 265, 664
Dufour R. J., Harvel C. A., Martins D. M., Schiffer F. H., III, Talent D. L., Wells D. C., van den Bergh S., Talbot R. J., Jr, 1979, AJ, 84, 284
Durrell P. R., Harris W. E., Pritchet C. J., 2001, AJ, 121, 2557
Eisenhardt P. R., De Propris R., Gonzalez A. H., Stanford S. A., Wang M., Dickinson M., 2007, ApJS, 169, 225
Elson R. A. W., 1997, MNRAS, 286, 771
Emsellem E., Dejonghe H., Bacon R., 1999, MNRAS, 303, 495
Emsellem E. et al., 2004, MNRAS, 352, 721
Erwin P., Sparke L. S., 2003, ApJS, 146, 299
Feldmeier J. J., Ciardullo R., Jacoby G. H., 1997, ApJ, 479, 231
Ferrarese L. et al., 2000, ApJS, 128, 431
Ferrarese L., Mould J. R., Stetson P. B., Tonry J. L., Blakeslee J. P., Ajhar E. A., 2007, ApJ, 654, 186
Fingerhut R. L., 2012, PhD thesis, York University.
Fingerhut R. L., McCall M. L., De Robertis M., Kingsburgh R. L., Komljenovic M., Lee H., Buta R. J., 2003, ApJ, 587, 672
Fingerhut R. L., Lee H., McCall M. L., Richer M. G., 2007, ApJ, 655, 814
Fisher D. B., Drory N., 2008, AJ, 136, 773
Fitzgibbons G. L., 1990, PhD thesis, Florida Univ., Gainesville
Fitzpatrick E. L., 1999, PASP, 111, 63
Flynn C., Holmberg J., Portinari L., Fuchs B., Jahreiß H., 2006, MNRAS, 372, 1149
Ford H. C., Hui X., Ciardullo R., Jacoby G. H., Freeman K. C., 1996, ApJ, 458, 455
Fraternali F., van Moorsel G., Sancisi R., Oosterloo T., 2002, AJ, 123, 3124
Freedman W. L. et al., 2001, ApJ, 553, 47

Freeman K. C., Karlsson B., Lynga G., Burrell J. F., van Woerden H., Goss W. M., Mebold U., 1977, A&A, 55, 445
Fry A. M., Morrison H. L., Harding P., Boroson T. A., 1999, AJ, 118, 1209
Galleti S., Bellazzini M., Ferraro F. R., 2004, A&A, 423, 925
García-Ruiz I., Sancisi R., Kuijken K., 2002, A&A, 394, 769
Garrido O., Marcelin M., Amram P., Boissin O., 2003, A&A, 399, 51
Gavazzi G., Boselli A., Donati A., Franzetti P., Scodeggio M., 2003, A&A, 400, 451
Gebhardt K. et al., 2000, AJ, 119, 1157
Gieren W., Pietrzyński G., Soszyński I., Bresolin F., Kudritzki R.-P., Storm J., Minniti D., 2008, ApJ, 672, 266
Gordon K. D., Clayton G. C., Misselt K. A., Landolt A. U., Wolff M. J., 2003, ApJ, 594, 279
Gottesman S. T., Davies R. D., 1970, MNRAS, 149, 263
Grocholski A. J. et al., 2008, ApJ, 686, L79
Harris G. L. H., Harris W. E., Poole G. B., 1999, AJ, 117, 855
Helmboldt J. F., Walterbos R. A. M., Bothun G. D., O'Neil K., de Blok W. J. G., 2004, ApJ, 613, 914
Heraudeau P., Simien F., 1996, A&AS, 118, 111
Héraudeau P., Simien F., Maubon G., Prugniel P., 1999, A&AS, 136, 509
Hernandez O., Carignan C., Amram P., Chemin L., Daigle O., 2005, MNRAS, 360, 1201
Herrmann K. A., Ciardullo R., Feldmeier J. J., Vinciguerra M., 2008, ApJ, 683, 630
Hlavacek-Larrondo J., Marcelin M., Epinat B., Carignan C., de Denus-Baillargeon M.-M., Daigle O., Hernandez O., 2011, MNRAS, 416, 509
Holmberg J., Flynn C., Portinari L., 2006, MNRAS, 367, 449
Huchtmeier W. K., Richter O. G., 1986, A&AS, 63, 323
Hui X., Ford H. C., Ciardullo R., Jacoby G. H., 1993, ApJ, 414, 463
Hui X., Ford H. C., Freeman K. C., Dopita M. A., 1995, ApJ, 449, 592
Hummel E., Dettmar R.-J., 1990, A&A, 236, 33
Humphreys E. M. L., Reid M. J., Moran J. M., Greenhill L. J., Argon A. L., 2013, ApJ, 775, 13
Hunter D. A., Elmegreen B. G., 2006, ApJS, 162, 49
Hunter D. A., Wilcots E. M., van Woerden H., Gallagher J. S., Kohle S., 1998, ApJ, 495, L47
Hunter D. A., van Woerden H., Gallagher J. S., 1999, AJ, 118, 2184
Hurt R. L., Turner J. L., Ho P. T. P., 1996, ApJ, 466, 135
Ibata R. A. et al., 2013, Nature, 493, 62
Ichikawa T., Yanagisawa K., Itoh N., Tarusawa K., van Driel W., Ueno M., 1995, AJ, 109, 2038
Jacoby G. H., Ciardullo R., Booth J., Ford H. C., 1989, ApJ, 344, 704
Jarrett T. H., Chester T., Cutri R., Schneider S. E., Huchra J. P., 2003, AJ, 125, 525
Jones K. L., Koribalski B. S., Elmouttie M., Haynes R. F., 1999, MNRAS, 302, 649
Kamphuis J., Briggs F., 1992, A&A, 253, 335
Kapranidis S., Sullivan W. T., III, 1983, A&A, 118, 33
Karachentsev I. D., 2005, AJ, 129, 178
Karachentsev I. D., Kutkin A. M., 2005, Astron. Lett., 31, 299
Karachentsev I. D. et al., 2002a, A&A, 383, 125
Karachentsev I. D. et al., 2002b, A&A, 385, 21
Karachentsev I. D. et al., 2003a, A&A, 398, 467
Karachentsev I. D. et al., 2003b, A&A, 398, 479
Karachentsev I. D. et al., 2003c, A&A, 404, 93
Karachentsev I. D., Karachentseva V. E., Huchtmeier W. K., Makarov D. I., 2004, AJ, 127, 2031
Karachentsev I. D. et al., 2006, AJ, 131, 1361
Karachentsev I. D. et al., 2007, AJ, 133, 504
Khare R. C., 1953, ZAp, 33, 251
Kim M., Kim E., Lee M. G., Sarajedini A., Geisler D., 2002, AJ, 123, 244
Kirby E. M., Jerjen H., Ryder S. D., Driver S. P., 2008, AJ, 136, 1866
Kiszkurno-Koziej E., 1988, A&A, 196, 26
Klypin A., Hoffman Y., Kravtsov A. V., Gottlöber S., 2003, ApJ, 596, 19
Koribalski B. S. et al., 2004, AJ, 128, 16
Kraan-Korteweg R. C., Tammann G. A., 1979, Astron. Nachr., 300, 181
Kroupa P., 1998, in Rebolo R., Martin E. L., Zapatero Osorio M. R., eds, ASP Conf. Ser. Vol. 134, Brown Dwarfs and Extrasolar Planets. Astron. Soc. Pac., San Francisco, p. 483
Kuno N., Nakai N., 1997, PASJ, 49, 279
Larson R. B., 1974, MNRAS, 169, 229
Lee B., Lee J., 2008, MNRAS, 389, 1001
Libeskind N. I., Hoffman Y., Knebe A., Steinmetz M., Gottlöber S., Metuki O., Yepes G., 2012, MNRAS, 421, L137
Longair M. S., 2008, Galaxy Formation. Springer, Berlin
Macri L. M., Huchra J. P., Sakai S., Mould J. R., Hughes S. M. G., 2000, ApJS, 128, 461
Macri L. M., Stanek K. Z., Bersier D., Greenhill L. J., Reid M. J., 2006, ApJ, 652, 1133
Makarova L., 1999, A&AS, 139, 491
Marcelin M., Athanassoula E., 1982, A&A, 105, 76
Marcum P. M. et al., 2001, ApJS, 132, 129
Mathews W. G., Baker J. C., 1971, ApJ, 170, 241
Matteucci F., Pipino A., 2002, ApJ, 569, L69
Mayya Y. D., Carrasco L., Luna A., 2005, ApJ, 628, L33
McCall M. L., 2004, AJ, 128, 2144
McCall M. L., Armour M.-H., 2000, in Kraan-Korteweg R. C., Henning P. A., Andernach H., eds, ASP Conf. Ser. Vol. 218, Mapping the Hidden Universe: The Universe behind the Milky Way – The Universe in H I, Astron. Soc. Pac., San Francisco, p. 1
McCall M. L., Richer M. G., 2003, in Kwok S., Dopita M., Sutherland R., eds, IAU Symp. Vol. 209, Planetary Nebulae: Their Evolution and Role in the Universe, p. 583
McCall M. L., Richer M. G., Stasińska G., 1998, in Friedli D., Edmunds M., Robert C., Drissen L., eds, ASP Conf. Ser. Vol. 147, Abundance Profiles: Diagnostic Tools for Galaxy History. Astron. Soc. Pac., San Francisco, p. 259
McConnachie A. W., Irwin M. J., Ferguson A. M. N., Ibata R. A., Lewis G. F., Tanvir N., 2004, MNRAS, 350, 243
McConnachie A. W., Irwin M. J., Ferguson A. M. N., Ibata R. A., Lewis G. F., Tanvir N., 2005, MNRAS, 356, 979
McKee C. F., Truelove J. K., 1995, Phys. Rep., 256, 157
McMillan P. J., 2011, MNRAS, 414, 2446
McMillan R., Ciardullo R., Jacoby G. H., 1994, AJ, 108, 1610
Moiseev A. V., Valdés J. R., Chavushyan V. H., 2004, A&A, 421, 433
Möllenhoff C., 2004, A&A, 415, 63
Mouhcine M., Ferguson H. C., Rich R. M., Brown T. M., Smith T. E., 2005, ApJ, 633, 810
Mould J., Sakai S., 2008, ApJ, 686, L75
Mould J., Sakai S., 2009, ApJ, 694, 1331
Murray N., Quataert E., Thompson T. A., 2005, ApJ, 618, 569
Neistein E., Maoz D., Rix H.-W., Tonry J. L., 1999, AJ, 117, 2666
Newton K., 1980a, MNRAS, 190, 689
Newton K., 1980b, MNRAS, 191, 169
Noordermeer E. et al., 2008, MNRAS, 384, 943
Norris M. A., Sharples R. M., Kuntschner H., 2006, MNRAS, 367, 815
Okamura S., Kanazawa T., Kodaira K., 1976, PASJ, 28, 329
Okamura S., Takase B., Kodaira K., 1977, PASJ, 29, 567
Oliva E., Marconi A., Moorwood A. F. M., 1999, A&A, 342, 87
Olling R. P., 1996, AJ, 112, 457
Oosterloo T., Fraternali F., Sancisi R., 2007, AJ, 134, 1019
Oppenheimer B. D., Davé R., 2006, MNRAS, 373, 1265
Ostriker J. P., Naab T., 2012, Phys. Today, 65, 43
Ott M., Whiteoak J. B., Henkel C., Wielebinski R., 2001, A&A, 372, 463
Pack D. C., 1953, MNRAS, 113, 43
Pasetto S., Chiosi C., 2007, A&A, 463, 427
Paturel G., Petit C., Prugniel P., Theureau G., Rousseau J., Brouty M., Dubois P., Cambrésy L., 2003, A&A, 412, 45
Peebles P. J. E., 1993, Principles of Physical Cosmology. University Press, Princeton
Peebles P. J. E., Nusser A., 2010, Nature, 465, 565
Peebles P. J. E., Phelps S. D., Shaya E. J., Tully R. B., 2001, ApJ, 554, 104
Pence W. D., 1980, ApJ, 239, 54

Pence W. D., 1981, ApJ, 247, 473
Pierce M. J., Tully R. B., 1992, ApJ, 387, 47
Pinsonneault S., Martel H., Pieri M. M., 2010, ApJ, 725, 2087
Pipino A., Matteucci F., 2004, MNRAS, 347, 968
Pisano D. J., Wilcots E. M., Elmegreen B. G., 2000, AJ, 120, 763
Portinari L., Sommer-Larsen J., Tantalo R., 2004, MNRAS, 347, 691
Portinari L., Flynn C., Holmberg J., Fuchs B., Jahreiss H., 2009, in Andersen J., Nordströaram B., Bland-Hawthorn J., eds, IAU Symposium, Vol. 254, p. 53
Puche D., Carignan C., Bosma A., 1990, AJ, 100, 1468
Puche D., Carignan C., Wainscoat R. J., 1991, AJ, 101, 447
Rand R. J., 1994, A&A, 285, 833
Reid M. J. et al., 2009, ApJ, 700, 137
Rejkuba M., Greggio L., Harris W. E., Harris G. L. H., Peng E. W., 2005, ApJ, 631, 262
Rekola R., Richer M. G., McCall M. L., Valtonen M. J., Kotilainen J. K., Flynn C., 2005, MNRAS, 361, 330
Riess A. G. et al., 2011, ApJ, 730, 119
Riess A. G. et al., 2012, ApJ, 752, 76
Rix H.-W. R., Kennicutt R. C., Jr, Braun R., Walterbos R. A. M., 1995, ApJ, 438, 155
Rizzi L., Tully R. B., Makarov D., Makarova L., Dolphin A. E., Sakai S., Shaya E. J., 2007, ApJ, 661, 815
Rogstad D. H., Chu K., Crutcher R. M., 1979, ApJ, 229, 509
Rubin V. C., Burstein D., Ford W. K., Jr, Thonnard N., 1985, ApJ, 289, 81
Ryder S. D., Dopita M. A., 1994, ApJ, 430, 142
Ryder S. D., Staveley-Smith L., Malin D., Walsh W., 1995, AJ, 109, 1592
Saha A., Claver J., Hoessel J. G., 2002, AJ, 124, 839
Sakai S., Madore B. F., 1999, ApJ, 526, 599
Sakai S. et al., 2000, ApJ, 529, 698
Sakai S., Ferrarese L., Kennicutt R. C., Jr, Saha A., 2004, ApJ, 608, 42
Salpeter E. E., 1955, ApJ, 121, 161
Sancisi R., Allen R. J., 1979, A&A, 74, 73
Schlegel D. J., Finkbeiner D. P., Davis M., 1998, ApJ, 500, 525
Schmidt K.-H., Boller T., 1992a, Astron. Nachr., 313, 189
Schmidt K.-H., Boller T., 1992b, Astron. Nachr., 313, 329
Schönrich R., Binney J., Dehnen W., 2010, MNRAS, 403, 1829
Schweizer F., 1977, ApJ, 211, 324
Schweizer F., 1978, ApJ, 220, 98
Scoville N. Z., Soifer B. T., Neugebauer G., Matthews K., Young J. S., Yerka J., 1985, ApJ, 289, 129
Seth A. C., Dalcanton J. J., de Jong R. S., 2005, AJ, 129, 1331
Shostak G. S., 1973, A&A, 24, 411
Shostak G. S., van der Kruit P. C., 1984, A&A, 132, 20
Silge J. D., Gebhardt K., Bergmann M., Richstone D., 2005, AJ, 130, 406
Simien F., Prugniel P., 2002, A&A, 384, 371
Skrutskie M. F. et al., 2006, AJ, 131, 1163
Soffner T., Mendez R. H., Jacoby G. H., Ciardullo R., Roth M. M., Kudritzki R. P., 1996, A&A, 306, 9
Sofue Y., 1997, PASJ, 49, 17
Sofue Y., Nakai N., 1993, PASJ, 45, 139
Sofue Y., Honma M., Omodaka T., 2009, PASJ, 61, 227
Soifer B. T., Helou G., Werner M., 2008, ARA&A, 46, 201
Soria R. et al., 1996, ApJ, 465, 79
Spillar E. J., Oh S. P., Johnson P. E., Wenz M., 1992, AJ, 103, 793
Statler T. S., Smecker-Hane T., 1999, AJ, 117, 839
Staveley-Smith L., Davies R. D., Kinman T. D., 1992, MNRAS, 258, 334
Stil J. M., Israel F. P., 2002, A&A, 392, 473
Strom K. M., Strom S. E., Jensen E. B., Moller J., Thompson L. A., Thuan T. X., 1977, ApJ, 212, 335
Swaters R. A., Balcells M., 2002, A&A, 390, 863
Swaters R. A., Sancisi R., van der Hulst J. M., 1997, ApJ, 491, 140
Talbot R. J., Jr, Jensen E. B., Dufour R. J., 1979, ApJ, 229, 91
Thim F., Tammann G. A., Saha A., Dolphin A., Sandage A., Tolstoy E., Labhardt L., 2003, ApJ, 590, 256
Tilanus R. P. J., Allen R. J., 1991, A&A, 244, 8
Tonry J. L., Dressler A., Blakeslee J. P., Ajhar E. A., Fletcher A. B., Luppino G. A., Metzger M. R., Moore C. B., 2001, ApJ, 546, 681
Tully R. B., 1974, ApJS, 27, 437
Tully R. B., Fisher J. R., 1987, Nearby Galaxies Atlas. University Press, Cambridge
Tully R. B., Verheijen M. A. W., Pierce M. J., Huang J.-S., Wainscoat R. J., 1996, AJ, 112, 2471
Tully R. B., Shaya E. J., Karachentsev I. D., Courtois H. M., Kocevski D. D., Rizzi L., Peel A., 2008, ApJ, 676, 184
Vaduvescu O., McCall M. L., Richer M. G., Fingerhut R. L., 2005, AJ, 130, 1593
van Albada G. D., 1980, A&A, 90, 123
van der Marel R. P., Fardal M., Besla G., Beaton R. L., Sohn S. T., Anderson J., Brown T., Guhathakurta P., 2012, ApJ, 753, 8
van Houten C. J., 1961, Bull. Astron. Inst. Netherlands, 16, 1
van Woerden H., van Driel W., Braun R., Rots A. H., 1993, A&A, 269, 15
Vega Beltrán J. C., Pizzella A., Corsini E. M., Funes J. G., Zeilinger W. W., Beckman J. E., Bertola F., 2001, A&A, 374, 394
Velander M. et al., 2014, MNRAS, 437, 2111
Verdes-Montenegro L., Bosma A., Athanassoula E., 2000, A&A, 356, 827
Verheijen M. A. W., 1997, PhD thesis, University of Groningen
Verheijen M. A. W., 2001, ApJ, 563, 694
Verheijen M. A. W., Sancisi R., 2001, A&A, 370, 765
Walterbos R. A. M., Kennicutt R. C., Jr, 1987, A&AS, 69, 311
Wevers B. M. H. R., van der Kruit P. C., Allen R. J., 1986, A&AS, 66, 505
Wilkinson A., Sharples R. M., Fosbury R. A. E., Wallace P. T., 1986, MNRAS, 218, 297
Wong T., Blitz L., Bosma A., 2004, ApJ, 605, 183
Woodley K. A., Harris W. E., Beasley M. A., Peng E. W., Bridges T. J., Forbes D. A., Harris G. L. H., 2007, AJ, 134, 494
Xue X. X. et al., 2008, ApJ, 684, 1143

This paper has been typeset from a TEX/LATEX file prepared by the author.